








Phosphate-dependent nuclear export via a non-classical NES class recognized by exportin Msn5

Received: 24 July 2024

Accepted: 27 February 2025

Published online: 16 March 2025



Ho Yee Joyce Fung ^{1,2}, Sanraj R. Mittal ³, Ashley B. Niesman ^{1,2},
Jenny Jiou ^{1,4}, Binita Shakya^{1,5}, Takuya Yoshizawa^{1,6}, Ahmet E. Cansizoglu^{1,7},
Michael P. Rout ³ & Yuh Min Chook ¹ 

Gene expression in response to environmental stimuli is dependent on nuclear localization of key signaling components, which can be tightly regulated by phosphorylation. This is exemplified by the phosphate-sensing transcription factor Pho4, which requires phosphorylation for nuclear export by the yeast exportin Msn5. Here, we present a high resolution cryogenic-electron microscopy structure showing the phosphorylated 35-residue nuclear export signal of Pho4, which binds the concave surface of Msn5 through two Pho4 phosphoserines that align with two Msn5 basic patches. These findings characterize a mechanism of phosphate-specific recognition mediated by a non-classical signal distinct from that for Exportin-1. Furthermore, the discovery that unliganded Msn5 is autoinhibited explains the positive cooperativity of Pho4/Ran-binding and proposes a mechanism for Pho4's release in the cytoplasm. These findings advance our understanding of the diversity of signals that drive nuclear export and how cargo phosphorylation is crucial in regulating nuclear transport and controlling cellular signaling pathways.

The regulation of gene expression in response to environmental stimuli hinges critically on the nuclear import and export of key components from signaling pathways like MAP kinase, TGF- β /SMAD, Hippo and others^{1–3}. These proteins undergo dynamic changes in their localization between the nucleus and the cytoplasmic, controlled by phosphorylation, which either facilitates or inhibits interaction with nuclear transport receptors of the Karyopherin- β family, also known as importins, exportins and biportins^{4–6}.

One such example is the *S. cerevisiae* (Sc) exportin Msn5 (also known as Kap142), which is homologous to human Exportin-5 (XPO5). At least 18 different proteins have been reported to be exported by Msn5, including transcription factors and other proteins involved in

response to nutrients and stress, and proteins involved in cell cycle maintenance^{7–24}. Phosphorylation and dephosphorylation of these factors regulate their nuclear-cytoplasmic localization and transcription functions. Msn5 recognizes phosphorylated cargoes for nuclear export, such as the phosphate-sensing transcription factor Sc Pho4⁷. Pho4, regulated by phosphorylation from the Cyclin-CDK Pho80-Pho85 kinase complex, requires phosphorylation at specific sites for binding Msn5 and subsequent nuclear export^{7,25–27}. However, until now, the precise Msn5-binding element, recognition mode and the mechanism linking phosphorylation to nuclear export have been unknown. Overall, understanding the broader mechanisms of nuclear export regulation by phosphorylation remains a significant challenge.

¹Department of Pharmacology, UT Southwestern Medical Center, Dallas, TX 75039, US. ²Department of Biophysics, UT Southwestern Medical Center, Dallas, TX 75039, US. ³Laboratory of Cellular and Structural Biology, The Rockefeller University, New York, NY 10021, US. ⁴Present address: The Walter and Eliza Hall Institute of Medical Research, 1G, Royal Parade, Parkville, Victoria 302, Australia. ⁵Present address: Department of Clinical, Diagnostic & Therapeutic Sciences, College of Allied Health Professions, University of Nebraska Medical Center, Omaha, NE 68198, US. ⁶Present address: Research Division, Chugai Pharmaceutical Co., Ltd, Kanagawa, Japan. ⁷Present address: EMD Serono Research & Development Institute, 45A Middlesex Turnpike, Billerica, MA 01821, US.

 e-mail: yuhmin.chook@utsouthwestern.edu

Exportins are thought to recognize their protein cargoes by binding to linear sequence elements known as nuclear export signals (NESs) that often occur within intrinsically disordered regions (IDRs) of cargoes or to the folded domains of cargoes^{4,28,29}. For example, the well-characterized Exportin-1 (XPO1 or CRM1) binds >1000 diverse functioning protein cargoes, many carrying the 8–15 residue long classical-NES (cNES) peptide which is rich in hydrophobic residues^{30–34}. Most other exportins recognize folded domains in their cargoes; for example, profilin-actin by Exportin-6³⁵, Importin- α by CSE1/CAS³⁶, folded RNAs by XPOT and XPO5^{37,38}, and various export cargo protein domains by biportins IPO13, XPO4 and XPO7^{39–41}. The only other exportin known to bind IDRs of cargoes, via an embedded but until now uncharacterized NES, is Msn5²⁶.

In this work, cryogenic electron microscopy (cryo-EM) analysis of Msn5 bound to Ran^{GTP} and phosphorylated Pho4 has revealed a 35-residue NES that binds in extended conformation to the concave surface of the flexible Msn5 solenoid. The Pho4 NES is anchored to Msn5 at two phospho-serine residues, which are surrounded by many small polar and hydrophobic residues that also make important interactions with the exportin. This study not only identifies a non-classical NES class for Msn5 distinct from the cNES recognized by XPO1 (previously the only characterized NES class) but also elucidates how a phosphorylated cargo is specifically recognized for nuclear export. These findings advance our understanding the mechanisms by which

phosphorylation regulates nuclear export and their broader implications for a multitude of key cellular signaling pathways and protein transport mechanisms.

Results and discussion

Mapping the Msn5-binding region of Pho4

The 312-residue Pho4 consists of a 240-residue IDR followed by a C-terminal helix-loop-helix domain^{42,43} (Fig. 1a and Supplementary Fig. 1a,b). The IDR contains a transactivation domain, an isoleucine-lysine (IK)-NLS that binds the importin Kap121, a putative oligomerization region, and two separate regions that recruit the Pho80-Pho85 kinase to phosphorylate five Pho4 serine residues within the IDR (Fig. 1a)^{27,42,44,45}. We generated GST-fusion constructs of full length (FL) and truncated Pho4 to identify the minimal Pho4 region that binds Msn5. These GST-Pho4 constructs were phosphorylated in vitro with recombinant Pho80-Pho85 kinase. GST-pPho4_{FL}, -pPho4_{1–155}, -pPho4_{1–200} and -pPho4_{1–255} efficiently pulled down Msn5 in the presence of Sc Ran^{GTP} (residues 1–179, Q71L) but GST-Pho4_{100–150} did not pull down Msn5 (Fig. 1b and Supplementary Fig. 1c). We selected Pho4_{1–200}, which contains both Pho80-binding regions and binds Msn5 like Pho4_{FL}, for further studies.

Fluorescence polarization (FP) analysis showed high-affinity binding of wild type or WT mNeonGreen(mNeonG)-pPho4_{3–200} to WT Msn5 (dissociation constants or K_D 25[14,43] nM; 95% confidence

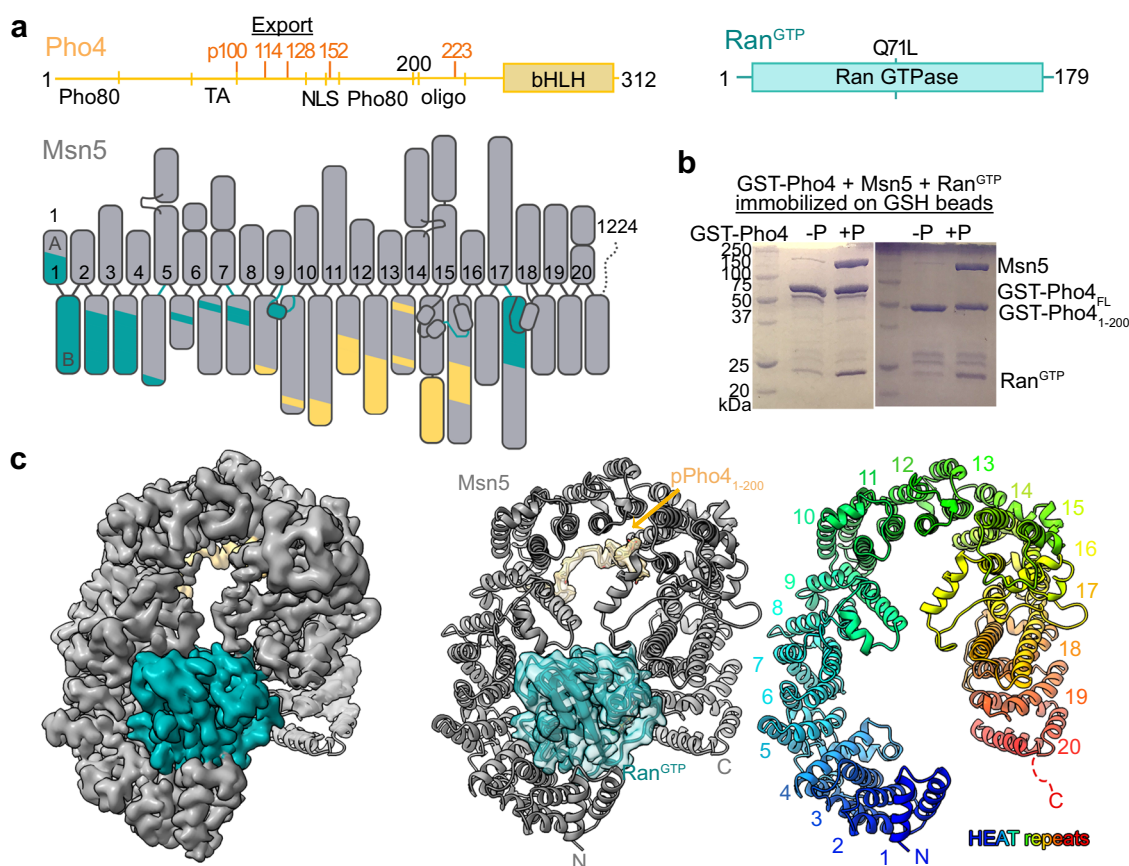


Fig. 1 | Cryo-EM structure of Msn5-Ran^{GTP}-pPho4. a Schematic of Pho4, Ran^{GTP} and Msn5. Pho4 has two Pho80-interacting regions (Pho80), a transactivation domain (TA), an IK-NLS, an oligomerization region (oligo) and five Pho85 phosphorylation sites (orange) in its IDR, and a C-terminal basic helix-loop-helix domain (bHLH). Each Msn5 helix is represented by a gray box scaled by its length; h9loop, h15loop and h17-h18loop contain small helices. HEAT repeats are numbered and regions that contact Ran^{GTP} or pPho4 are cyan or yellow, respectively. **b** Immobilized GST-Pho4_{FL} and -Pho4_{1–200}, in vitro phosphorylated (+P) or unphosphorylated (-P),

were mixed with Msn5 and excess Ran^{GTP} followed by extensive washing. Bound proteins were visualized by Coomassie stained SDS-PAGE. Representative image from triplicate experiment is shown. Source data are provided as a Source Data file. **c** The final map (left) and two cartoon representations of the Msn5 (gray) -Ran^{GTP} (cyan) -pPho4_{1–200} (wheat) structure (center and right). Map features for Ran^{GTP} and pPho4 are shown in the center panel, and Msn5 is in rainbow colors with HEAT repeats labeled in the right panel.

interval in brackets) (Supplementary Fig. 1d,e). The interaction of mNeonG-pPho4_{FL} with WT Msn5 showed 2-site binding, with K_{DS} of 10[U,90] nM (U = undetermined) and 400[200,2200] nM, consistent with a dimeric Pho4_{FL} binding with high affinity to Msn5 (Supplementary Fig. 1d, e).

Cryo-EM maps of pPho4₁₋₂₀₀ and pPho4_{FL} bound Msn5 reveal Msn5 flexibility

We purified ternary complexes of Msn5-Ran^{GTP}-pPho4₁₋₂₀₀ and Msn5-Ran^{GTP}-pPho4_{FL} for cryo-EM structure determination. We solved three 3.0–3.2 Å resolution structures of the former and obtained a 4.9 Å resolution map of the latter (Fig. 1c, Table 1, Supplementary Fig. 2–4 and Supplementary Table 1). 3D reconstruction of Msn5-Ran^{GTP}-pPho4₁₋₂₀₀ particles showed the 20 HEAT repeats (h1–h20; each with antiparallel A and B helices) of the horseshoe-shaped Msn5 solenoid, with Ran^{GTP} bound to its N-terminal repeats (Supplementary Movie 1).

Map features for bound pPho4 can be observed at the concave surface of Msn5 in all the Msn5-Ran^{GTP}-pPho4₁₋₂₀₀ and Msn5-Ran^{GTP}-pPho4_{FL} maps, but their extent and continuity vary across the maps (Supplementary Fig. 6). The most compact states of both complexes are very similar, have the strongest and most continuous Pho4 features, and are described below. The variable Msn5 solenoid and Pho4 conformations in the different maps, all from a single cryo-EM sample, suggest dynamic Pho4-Msn5 interactions with the flexible Pho4 polypeptide adapting to bind Msn5 solenoids of variable curvatures.

A 35-residue NES of Pho4 binds the central concave surface of Msn5

We focused our structural analysis on the 3.0 Å resolution structure of the most compact state of the Msn5-Ran^{GTP}-pPho4₁₋₂₀₀ complex (Fig. 1c). We built Msn5 HEAT repeats h1–h19 with confidence and placed its h20 by alignment into less well-defined density (Supplementary Fig. 3). The 20 HEAT repeats of Msn5 include a few unusually large HEAT repeats (h14, h15 and h17) and long loops (h9loop, h15loop and h17-h18loop) (Fig. 1a, c). The mode of Msn5-Ran^{GTP} binding is like that of other Kaps⁴: Msn5 h1–h3 repeats bind the Ran^{GTP} switch II, h4–h9 and h9loop bind the Ran^{GTP} basic patch, while h15loop and h17 bind Ran switch I (Supplementary Fig. 7).

Strong and continuous map features adjacent to the concave surface of Msn5 B helices of h8–h15 allowed confident modeling of 23 Pho4 residues that form three 90° related segments of a zig-zagging chain (Fig. 2a–c and Supplementary Fig. 8). The bound Pho4 residues 112–134 form a large and sprawling 1256.9 Å² interface with Msn5. This Pho4 segment is likely the persistently bound core portion of the Pho4 NES. The same Pho4 segment is resolved in the most compact Msn5-Ran^{GTP}-pPho4_{FL} map despite the lower resolution map (Fig. 2d and the State 1 map shown in Supplementary Fig. 4). This map shows additional Pho4 features beyond the N-terminal most of Pho4 residues modeled (L112) in the Msn5-Ran^{GTP}-pPho4₁₋₂₀₀ map, that is adjacent to a basic patch at the B helices of Msn5 repeats h16–h18 (Fig. 2d). We propose that Pho4 residues 100–111 occupy this density as mutating the electronegative ¹⁰²ATTAT¹⁰⁷ Pho4 segment to the basic GKKGKK decreased Msn5 affinity by 6-fold ($K_D = 110[70,150]$ nM for 102–107_{GKK} *vs* 20[12,31] nM for WT Pho4) (Fig. 2e, and all affinity data is summarized in Supplementary Table 2). Altogether, cryo-EM results reveal a Pho4 NES spanning residues 100–134 that zigzags along the B helices of Msn5 h8–h18 in an overall opposite direction to the solenoid (Fig. 2b).

The four regions of the Msn5-bound Pho4 NES

We divided the 35-residue Pho4 NES into four regions based on the locations of the three 90° turns of the zig-zagging chain (Fig. 2a, b). From the N-terminus, ¹⁰⁰SPATTATIKPRL¹¹¹ (NES region 1) binds dynamically to the basic patch at Msn5 h16–h18 (Fig. 2d). The peptide then makes a 90° turn at Pho4 L112 and ¹¹²LYPSLIHTQ¹²⁰ (NES region

2) binds in a shallow basic/hydrophobic Msn5 groove formed by HEAT repeats h12–h15 (Fig. 2c, right panel). The Pho4 chain makes a second -90° turn at ¹²⁰QS¹²¹ placing ¹²²AVPVTI¹²⁷ (NES region 3) over a hydrophobic patch formed by Msn5 helices h10B, h11B and h12B (Fig. 2c, middle panel). A third -90° turn at pS128 places the ¹²⁸PSPNLVAT¹³⁴ region (NES region 4) approximately parallel to the adjacent basic and acidic surfaces of Msn5 h8–h10 (Fig. 2c, left panel).

Although the structures clearly show phosphorylated Pho4 100–134 bound to Msn5, a Pho4 construct of these residues is insufficient for Msn5 binding because it is missing the kinase binding sites and therefore cannot be phosphorylated efficiently. Synthetic phosphopeptides were unsuitable for binding studies because of aggregation. Furthermore, phosphomimic mutations unfortunately do not substitute for Pho4 phosphorylation: Pho4₁₋₂₀₀ S114/128_{DD} and Pho4₁₋₂₀₀ S114/128_{EE} bind Msn5 weakly, like unphosphorylated Pho4₁₋₂₀₀, with $K_{DS} \sim 2$ –3 μM (Supplementary Fig. 9a). The ineffectiveness of these phosphomimic mutations suggests that the phosphate groups of pS114 and pS128 bind Msn5 via hydrogen-bonding rather than through charged-charged or electrostatic interactions. Though inconvenient, this finding is not entirely surprising as the efficacy of phosphomimic mutations is often case-dependent^{46–49}.

Msn5 interactions involving Pho4 pS114 and pS128

Phospho-serines pS114 and pS128 were previously reported to be critical for Msn5-mediated nuclear export²⁶. The phosphate moiety of Pho4 pS114 interacts with side chains of Msn5 residues H652, R754, Y863 and Y867 within repeats h13–h15 while pS128 interacts with three R393, R458 and R520 side chains within Msn5 h8–h10 (Fig. 3a). Mutation of Pho4 S114 or S128 to alanine decreased Msn5 binding affinity by 6- and 3-fold respectively ($K_D = 250[170,370]$ nM for S114_A and 120[90,160] nM for S128_A *vs* 44[26,71] nM for WT; Fig. 3b, left panel). Mutating both serines (S114/128_{AA}) decreased affinity 23-fold (K_D 1[0.7,1.4] μM), which is -2-fold tighter than unphosphorylated pPho4 (K_D 2.4[1.9,3.2] μM) (Fig. 3b, left panel and Supplementary Fig. 9a). This led us to examine the two remaining phosphoserines pS100 and pS152 that are not observed in the structure. Mutation of S100/152 to alanines decreased affinity by 2-fold ($K_D = 46[38,56]$ nM for S100/152_{AA} *vs* 20[12,31] nM for WT; Supplementary Fig. 9b). Altogether, these mutagenesis/binding affinity studies show that phosphorylation of Pho4 S114 and S128 is key for Msn5-binding while phosphorylation of S100 and S152 contributes minimally.

We also mutated the pS114-binding Msn5 residues (H652, R754, Y867 or the Msn5 HRY site; HRY_{AAA}) and the pS128-binding Msn5 residues (R393 and R458 or the Msn5 RR site; RR_{AA}). Both mutants bound pPho4 weaker: Msn5 HRY_{AAA} bound 5-fold weaker (K_D 230[160,350] nM) and Msn5 RR_{AA} bound 50-fold weaker (K_D 2.2[1.0,6.1] μM) (Fig. 3b, right panel). This shows that while both Msn5 phosphate-binding hotspots HRY and RR are important for pPho4 binding, RR is the stronger of the two.

The 5-fold affinity decrease of the Msn5 HRY_{AAA} mutant compared to Msn5 WT matches the 6-fold decrease seen for pPho4 S114A over pPho4 WT. However, the 50-fold affinity decrease of Msn5 RR_{AA} compared to the 3-fold decrease of pPho4 S128A is surprising as the two Msn5 arginine residues (R393 and R458) contact only the phosphate group of pS128 in the structure (Fig. 2c, left panel). It is possible that the loss of the phosphate group in pPho4 S128A is less detrimental because Msn5 R393 and R458 may still interact with the alanine at position 128 or its neighboring residues. Alternatively, in the absence of pS128, pS114 may bind at the Msn5 RR site (additional analysis in Supplementary Note 1). Analysis of the binding of Msn5 mutants with pPho4 mutants is also described in Supplementary Note 2.

In summary, the cryo-EM structure shows that Pho4 pS114 binds at the Msn5 HRY site, and pS128 binds at the Msn5 RR site. Mutagenesis/affinity analyses validate these interactions and show that at least one of the Pho4 phosphoserines is needed for sub-micromolar affinity

Table 1 | Cryo-EM data, map and model statistics of Msn5-Ran^{GTP}-pPho4₁₋₂₀₀ and unliganded Msn5

	Msn5-Ran ^{GTP} -pPho4 ₁₋₂₀₀		Msn5
	State 1-1 (EMD-46549) (PDB 9D45)	State 2-1 (EMD-47291) (PDB 9DXM)	State 3-1 (EMD-47325) (PDB 9DZ6)
Data collection and processing			
Magnification	105,000		81,000
Voltage (kV)	300		300
Electron exposure (e ⁻ /Å ²)	50		50
Defocus range (μm)	-0.8 to -2.5		-0.8 to -2.5
Pixel size (Å)	0.83		1.02885
Symmetry imposed	C1		C1
Initial particle images after 1 st clean-up (no.)	1,574,329		4,135,768
Final particle images (no.)	102,030	102,289	112,923
Map resolution (Å)	3.08	3.19	3.11
FSC Threshold	0.143	0.143	0.143
Map resolution range (Å)	2.62-6.67	2.80-6.72	2.68-6.16
B factor (Å ²)	89.9	90.7	89.3
			174.5
Refinement			
Initial model used	Msn5 and Ran ^{GTP} from 3m1l		
Model resolution (Å)	2.9/3.0/3.2	3.0/3.2/2.3	3.0/3.1/3.2
FSC threshold	0/0.143/0.5	0/0.143/0.5	0/0.143/0.5
Model composition			
Nonhydrogen atoms	11123	10056	10126
Protein residues	1354	1224	1232
Ligand	2 (GTP, Mg)	2 (GTP, Mg)	2 (GTP, Mg)
B factors (Å ²)			
Protein	30.00/469.43/159.44	30.00/215.68/113.42	30.00/249.07/144.89
Ligand	136.33/148.85/143.99	133.09/172.98/157.80	149.57/184.59/170.08
R.m.s. deviations			
Bond lengths (Å)	0.003	0.006	0.004
Bond angles (°)	0.610	0.596	0.487
Validation			
MolProbity score	1.33	1.26	1.35
Clashscore	5.43	3.86	5.04
Poor rotamers (%)	0.72	0.00	0.26
Ramachandran plot			
Favored (%)	97.84	97.60	97.60
Allowed (%)	2.16	2.40	2.31
Disallowed (%)	0.00	0.00	0.08
Missing residues	Msn5: 1-4, 1165-1224; Ran: 1-9; Pho4: 1-111, 135-200	Msn5: 1-4, 827-844, 962-977, 1006-1014, 1070-1071, 1087-1100, 1117-1224; Ran: 1-9; Pho4: 1-200	Msn5: 1-5, 826-845, 962-977, 1003-1016, 1070-1072, 1088-1098, 1118-1119, 1128-1224; Ran: 1-9; Pho4: 1-200

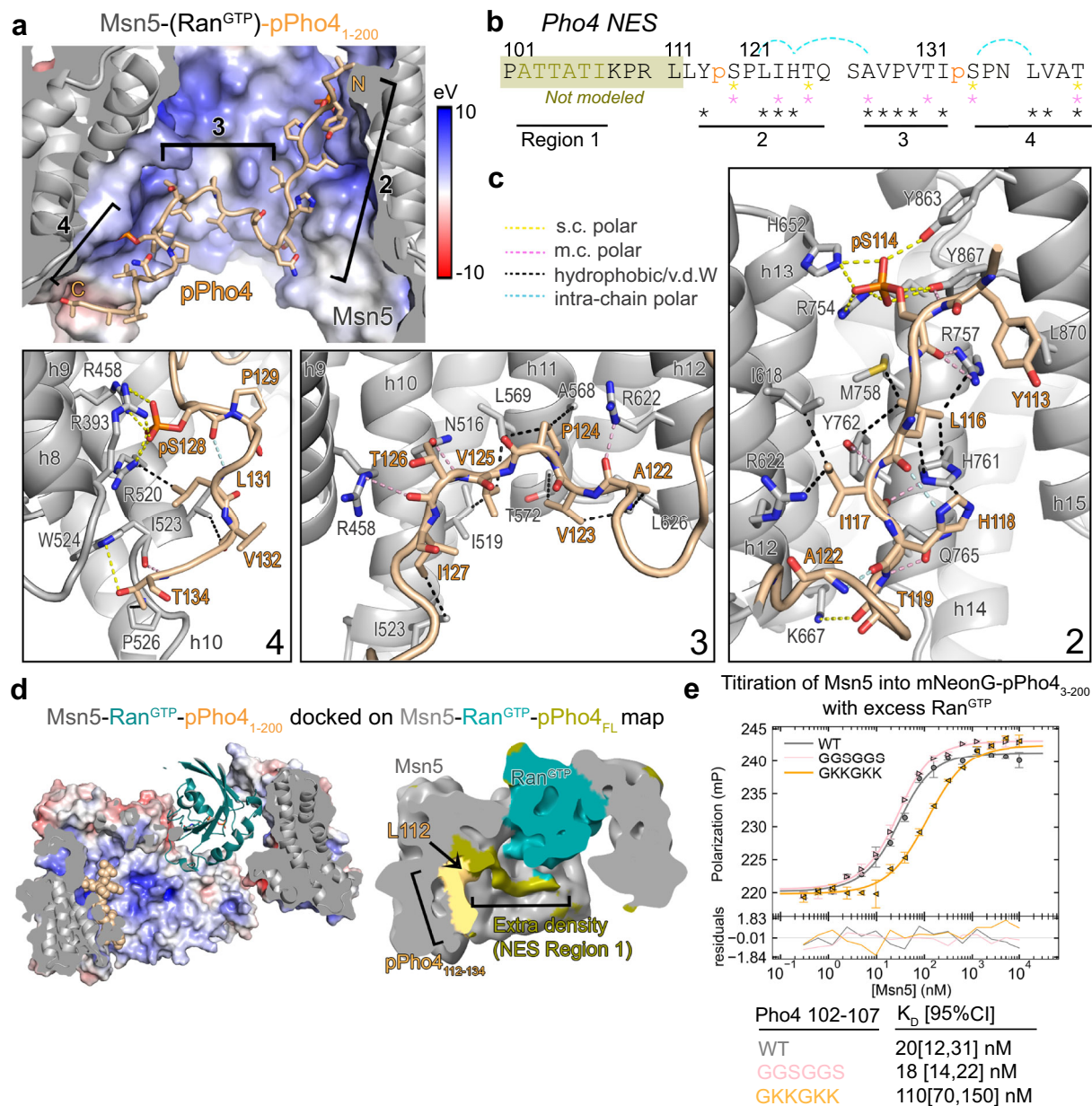


Fig. 2 | pPho4 NES binds to the central concave surface of Msn5. a Msn5 bound to pPho4₁₁₂₋₁₃₄ (wheat cartoon; regions 2–4 labeled). Msn5 electrostatic surface potential (red to blue: -10 to 10 eV; same in (d)). **b** The pPho4 NES sequence (regions 1–4 labeled) with Msn5 contacts represented by yellow, pink, and black asterisks - side chain polar, main chain polar and hydrophobic contacts respectively, blue dotted lines - intra-chain polar. Residues in olive box were not modeled. **c** Details of pPho4 NES regions 2–4, with contacts shown as dotted lines in same color scheme as (b). **d** State 1 map of Msn5-Ran^{GTP}-pPho4_{FL} (right) colored as in the docked Msn5-

Ran^{GTP}-pPho4₁₋₂₀₀ structure (left, in the same orientation, colored as in (a), pPho4 in spheres). Extra continuous density N-terminal of the pPho4₁₁₂₋₁₃₄, likely occupied by Pho4 NES region 1, is colored in olive. **e** FP titration of Msn5 into mNeonG-Pho4₃₋₂₀₀ with excess Ran^{GTP}. Residues 102–107 (NES region 1) were mutated to GGSGGS or GKKGKK. Data points are mean ± s.d. from triplicates, line represent 1-site binding and fitting residuals are plotted below. Source data are provided as a Source Data file.

pPho4-Msn5 binding. Interactions at the Msn5 RR site contribute more binding energy than the Msn5 HRY site.

Transcription factor cargoes binding to Msn5 HRY and RR sites regulates expression of downstream genes

To examine the functional relevance of these in vitro findings in vivo, we first attempted plasmid overexpression of the Pho4-GFP fluorescent nuclear export reporter while also expressing either WT Msn5 or Msn5 HRYRR_{AAAAA}, a Msn5 construct with both phosphate-binding HRY and RR hotspots mutated. Unfortunately, dramatic variability in expression levels of both the reporter cargo and the exportin

precluded reliable quantification of the nuclear-cytoplasmic localization results. Consistent with previous reports that Msn5 overexpression results in a slower growth phenotype^{50–52}, we found that overexpression of both WT and HRYRR_{AAAAA} Msn5 proteins were equally deleterious to cell growth (Supplementary Fig. 10). We therefore took the alternative approach to grow the two Msn5 strains to mid-log growth phase and extract their total RNA for mRNA sequencing (Fig. 4).

Gene expression changes, comparing the empty vector control strain to the WT Msn5 strain and comparing the HRYRR_{AAAAA} mutant strain to the WT Msn5 strain, were determined and plotted. Our in vitro

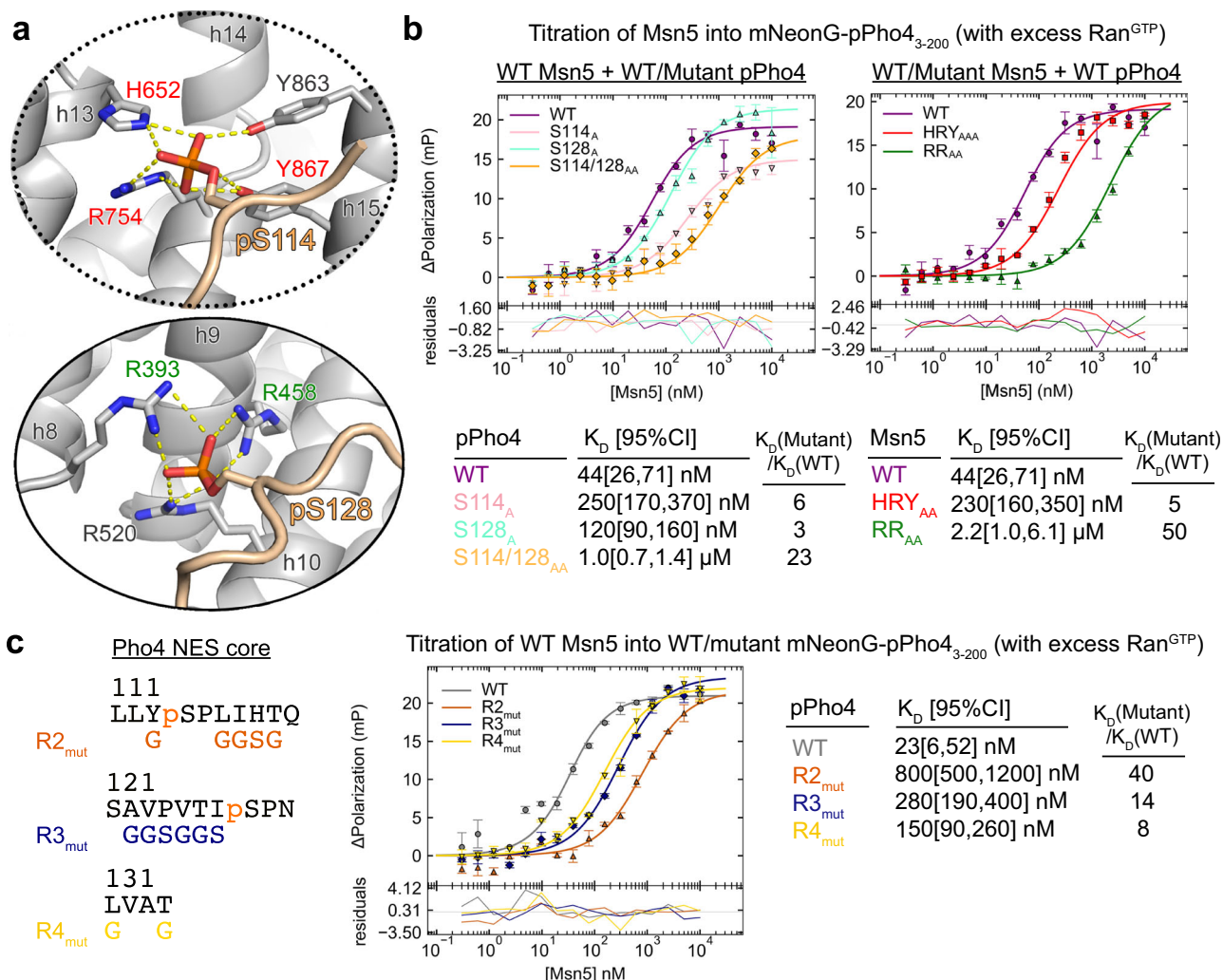


Fig. 3 | Pho4 phosphates and hydrophobic/polar side chains contribute to high affinity pPho4-Msn5 interactions. **a** Msn5 residues that contact pS114 and pS128. Residues mutated in Msn5 HRV_{AAA} are labeled in red and those in Msn5 RR_{AA} are in green. **b** Left: FP assays of WT Msn5 binding to mNeonG-pPho4₃₋₂₀₀ (WT and S114/S128 mutants) in the presence of excess Ran^{GTP}. Right: WT, HRV_{AAA} and RR_{AA} Msn5

binding to WT mNeonG-pPho4₃₋₂₀₀ with excess Ran^{GTP}. Data points represent mean \pm s.d. of triplicate measurements. Lines represent 1-site binding fits and residuals are plotted below. Dissociation constants (K_D) are shown with 95% confidence interval in brackets. Source data are provided as a Source Data file. **c** As in left panel of **b**, but with pPho4 NES mutated in regions 2-4, as indicated on the left.

analyses had indicated that the Msn5 protein in the mutant strain should be incompetent for Pho4-binding, and nuclear export of Pho4 and other Msn5 transcription factor cargoes that bind at the Msn5 HRV and RR sites should be nearly abolished. As such, in both the empty vector control and the mutant strain, transcription factor cargoes should remain in the nucleus and the resulting expression of genes under the control of these transcription factors should increase.

Beginning with the Pho4 transcription factor (Fig. 4a, d), genes downstream show a general trend towards overexpression as compared to the WT Msn5 strain in both the Empty Vector and HRVRR_{AAAAA} mutant conditions. When this same analysis is applied to another cargo of Msn5, the Mig1 transcription factor⁹, we see the same general trend towards overexpression in both the empty vector and mutant strains (Fig. 4b, e). Finally, as a control, we plotted the genes downstream of Pip2 (Fig. 4c, f), a transcription factor that does not bind Msn5, and there is no discernible trend in either condition.

The expression of the binding incompetent double mutant results in a similar trend of increased expression of genes under the control of its cognate cargoes as does expressing an empty vector in an Msn5 knockout background. We have also shown that these effects are not generalized across all transcription factors but are limited specifically to those that are directly exported from the nucleus by Msn5. In

summary, this RNAseq analysis has validated the critical functional importance of the HRV and RR binding pockets in yeast and has also highlighted an important function of Msn5 in regulating gene expression.

Hydrophobic and polar side chains of the Pho4 NES contribute to Msn5-binding

Fourteen other non-phospho-serine residues within the Pho4 NES core also make extensive interactions with Msn5 (Fig. 2b, c). The side chains of NES region 2 (¹¹³YpSPLIHTQ¹²⁰) make numerous hydrophobic interactions with side chains of the B helices of Msn5 h12-h15, while the Pho4 main chain makes many polar interactions with Msn5 (Fig. 2c, right panel). Interacting Msn5 residues here are mostly hydrophobic or basic. Additionally, intramolecular Pho4 interactions, such as between the main chain carbonyl of H118 with the main chain amide of A122 likely stabilizes the 90° turn of the Pho4 chain. Mutating all the non-phospho-serine Msn5-interacting residues in region 2 to generate the R2_{mut} (¹¹³YpSPGGSG; glycine and serine residues were chosen to preserve intrinsic disorder of the Pho4 segment) decreased Msn5-binding by 40-fold (K_D 800[500,1200] nM; Fig. 3c), underscoring the substantial contributions of these non-phospho-serine residues to Msn5 binding (Fig. 3b).

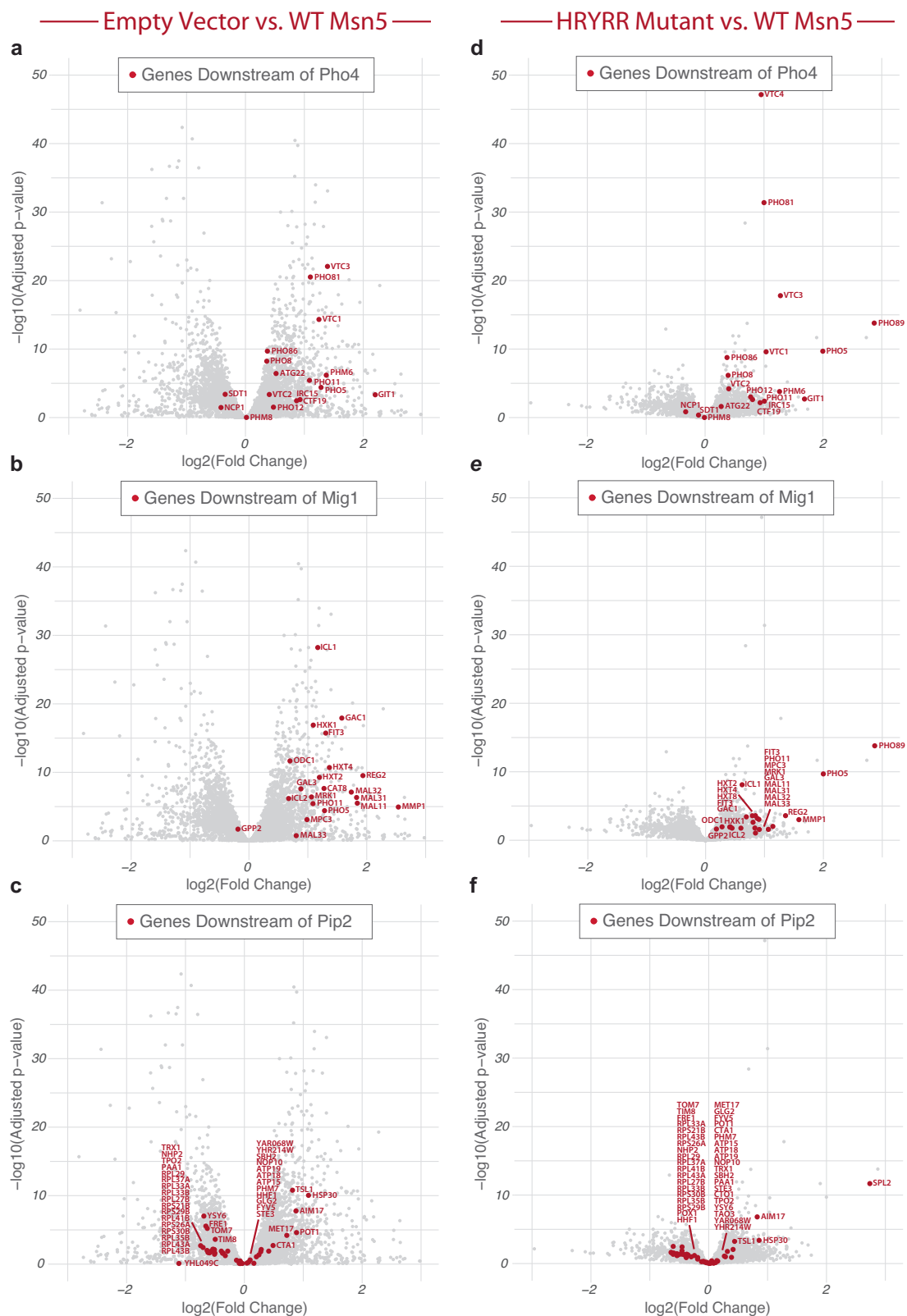


Fig. 4 | Genes downstream of Msn5 transcription factor cargoes show similar pattern of expression changes in Msn5 knockout and HRYRR_{AAAAA} mutant strains. a–c Volcano plots comparing Empty Vector (Msn5 KO) gene expression to *Msn5* WT gene expression. **d–f** Volcano plots comparing *Msn5* HRYRR_{AAAAA} mutant strain gene expression to WT *Msn5* gene expression. Genes downstream of the

transcription factors Pho4 (a, d), Mig1 (b, e), and Pip2 (c, f) are highlighted in red. Source data are provided as a Source Data file. DESeq2 performs two-sided Wald test, corrected for multiple comparisons using the Benjamini and Hochberg method.

Every Pho4 side chain in NES region 3, ¹²²AVPVTI¹²⁷, contacts Msn5 (Fig. 2c, middle panel). The small hydrophobic side chains of Pho4 residues 122–125 make hydrophobic interactions with Msn5 side chains in h10–h12, and both ends of the NES region 3 main chains make polar interactions with Msn5 arginine side chains. Intramolecular Pho4 interactions are also present, with the V123, V125, and I127 side chains lining up on one side of the Pho4 chain, contacting each other. Mutating ¹²²AVPVTI¹²⁷ to GGSGGS (R3_{mut}) decreased affinity 14-fold (K_D 280[190,400] nM; Fig. 3c), supporting the importance of these side chains in binding Msn5.

Pho4 NES region 4 (¹²⁸pSPNLVAT¹³⁴) contacts the B helices of Msn5 helices h8–h10 (Fig. 2c, left panel). ¹²⁸pSPNL¹³¹ forms a turn held by intramolecular hydrogen bond-like contacts, which position pS128 and L131 onto a basic patch at the Msn5 RR site. Residues before and after the turn also interact with Msn5 residues. Mutations of the only non-phospho-serine side chains here that contact Msn5, Pho4 L131A/T134A (R4_{mut}), decreased affinity by 8-fold (K_D 150[90,260] nM; Fig. 3c), supporting their importance in Msn5-binding.

In summary, many hydrophobic and small polar side chains in each of Pho4 NES regions 2, 3 and 4 contribute substantially to total binding energy. They are as important as phosphoserines pS114 and pS128 for high-affinity Msn5-binding. Importantly, many Pho4–Msn5 contacts also involve the Pho4 main chain.

Characteristics of the Pho4 NES and its binding site on Msn5

Structural analysis shows a 35-residue Pho4 NES that zigzags across a long contiguous interface on the concave and hydrophobic/basic surface that spans HEAT repeats h8–h18 of Msn5. The Pho4 NES includes the dynamic N-terminal region 1 followed by the persistently bound core of regions 2–4. Sixteen of the 23 Pho4 NES core residues contact Msn5. These include two critical phosphoserines pS114 and pS128 positioned 30 Å apart into two binding hotspots of Msn5 (HRY and RR sites), and many hydrophobic and small polar side chains that are also important for binding. The Pho4 NES also uses many main chain atoms across the NES to bind Msn5. Furthermore, intramolecular hydrogen bond-like contacts within the NES enable the chain to make the three sharp turns to stay close to the curved Msn5 interface. ConSURF analysis of 101 fungal Msn5 homologs show that 79% (37 of 43) of the residues that make up the Pho4-binding interface are conserved, consistent with their roles in binding Pho4 and likely other Msn5 cargoes (Supplementary Fig. 11).

We compared our cryo-EM structure to AlphaFold3 (AF3)⁵³ models predicted with Msn5, Ran^{GTP} and either Pho4_{1–200} or Pho4_{FL} (detailed analysis in Supplementary Note 3 and Fig. 12). AF3 predicted the structure of Ran-bound Msn5 but not the Msn5–Pho4 binding mode observed in our structure. When using Pho4_{1–200}, the predictor placed Pho4 pS100 and pS152 rather than pS114 and pS128 into the Msn5 HRY and RR sites, respectively. Some of the predictions using Pho4_{FL} placed the phosphates of pS114 and pS128 correctly, but others placed the wrong phosphoserines at the HRY or RR sites. Interestingly, the top scoring AF3 models fared worse than lower scoring models in placing the correct Pho4 phosphoserines at the Msn5 HRY and RR sites. None of the AF3 models accurately predicted the Pho4 conformation/path spanning NES regions 2–4 nor the placement of NES region 1 at the acidic patch of Msn5.

Based on the Pho4 NES and Msn5 features observed in our cryo-EM structures, we propose that the following NES characteristics may be generally important for binding Msn5: 1) Location in an IDR. 2) Two potential phosphorylation sites spaced 10 residues or more to span the 30 Å between the Msn5 HRY and RR sites. 3) Enrichment in aliphatic hydrophobic and small polar side chains. 4) Few or no basic residues since the Pho4-binding site of Msn5 is basic.

We examined sequences within the regions of the other Msn5 cargoes that had been reported to be important for nuclear export^{7–24}. Nine of the 17 Msn5 cargoes contain sequences that seem to fit the

criteria noted above (Supplementary Data 1). Future studies using appropriate kinases and various mapped cargo fragments will be needed to test these putative NESs for Msn5-binding and nuclear export.

We also note that the prediction of Msn5-binding NESs is likely further complicated by the likelihood that Msn5–NES binding modes and the sequences/structures of the NESs might be quite diverse. The Pho4 NES binding site that spans HEAT repeats h8–h15 of Msn5 is large and open, and Pho4 pS114 and pS128 bind only two (Msn5 HRY and RR sites) of the four basic patches on this Msn5 surface. Additional Msn5 basic patches at nearby Msn5 residues K561/K562 and R450/R454 may bind phospho-serine/threonine residues of other cargoes (Supplementary Fig. 13). The combinatorial use of four basic potential phosphate-binding sites could result in very diverse modes of Msn5 binding to phosphorylated NESs. The extent of structural and sequence diversity of NESs that bind at repeats h8–h18 of Msn5 will only be evident with additional cargo-bound structures.

Cargo recognition by Msn5 vs XPO5

Msn5 and its human homolog XPO5 share 21% sequence identity. Alignment of the cargo-bound exportin structures using the DALI server⁵⁴ shows similar HEAT repeat organization and architecture (Supplementary Fig. 14). Many yeast and human Kap homologs share conserved cargo specificities, but Msn5 is known to export phosphorylated proteins while XPO5 exports pre-miRNAs^{55–59}. Both XPO5 and Msn5 were reported to export tRNAs and XPO5 was reported to also export dsRNA-binding proteins. It is unclear if XPO5 binds those proteins directly or via their common RNA ligands^{60–68}.

Alignment of the Msn5 and XPO5 structures shows that both exportins use their concave surfaces at h8–h19 to bind Pho4 and pre-miRNA, respectively (Fig. 5a). However, the binding sites overlap only partially. Furthermore, only 11 of 27/41 Msn5/XPO5 residues that bind Pho4/pre-miRNA are in common and only three Msn5 residues that contact Pho4 are conserved in XPO5 (Supplementary Fig. 14). All three residues, R393, R458 and R520, are part of the dominant phosphate-binding hotspot that binds Pho4 pS128, the Msn5 RR site, while the equivalent arginine residues in XPO5 (R380, R448 and R519) interact with the dsRNA stem (Fig. 5b). While the Msn5 RR site is conserved in XPO5, the Msn5 HRY site is not. Overall, only ~30% of the residues that contact Pho4 or pre-miRNA are similar/identical in Msn5/XPO5. Partial conservation of the cargo binding mode in Msn5 and XPO5 suggests a partial conservation of their protein cargo/NES specificities.

The Pho4 NES bears no resemblance to the cNES that binds XPO1

The NES of Pho4 is strikingly different from the cNESs that bind XPO1 (Figs. 1c, 2a, 5c, d). They differ in several ways: 1) The much longer 35-residue Pho4 NES core adopts an extended conformation when bound to Msn5, while the 8–15 residue cNESs adopt diverse helix-loop structures when bound to XPO1^{30–34}. 2) The Pho4 NES binds to a large, flexible and basic binding site on the concave side of the Msn5 solenoid, whereas cNESs bind to an invariant hydrophobic groove on the convex side of the XPO1 solenoid. 3) The binding energy for Msn5–Pho4 interactions is distributed across 4 regions spanning 35 amino acids of the NES and involves two phosphoserine anchors. In contrast, cNES–XPO1 interactions are anchored by 4–5 hydrophobic side chains within a compact ~8–15 residues long peptide^{30,32,69}. 4) Msn5 binds pPho4 with low nanomolar affinity and Msn5/Pho4 mutants that bind at low micromolar affinities are no longer active for nuclear export²⁶. In contrast, the cNES–XPO1 affinity range for active nuclear export is large, spanning low nanomolar to tens of micromolar⁷⁰.

The long Pho4 NES, with its complex and vague sequence features that seem required for binding Msn5 and distribution of energetic interactions across several segments, bears similarities to the proline-tyrosine (PY) NLSs, which are recognized by the importin TNPO1/Kapβ2^{71,72}. Like the PY-NLS, which uses 3–4 NLS epitopes to interact

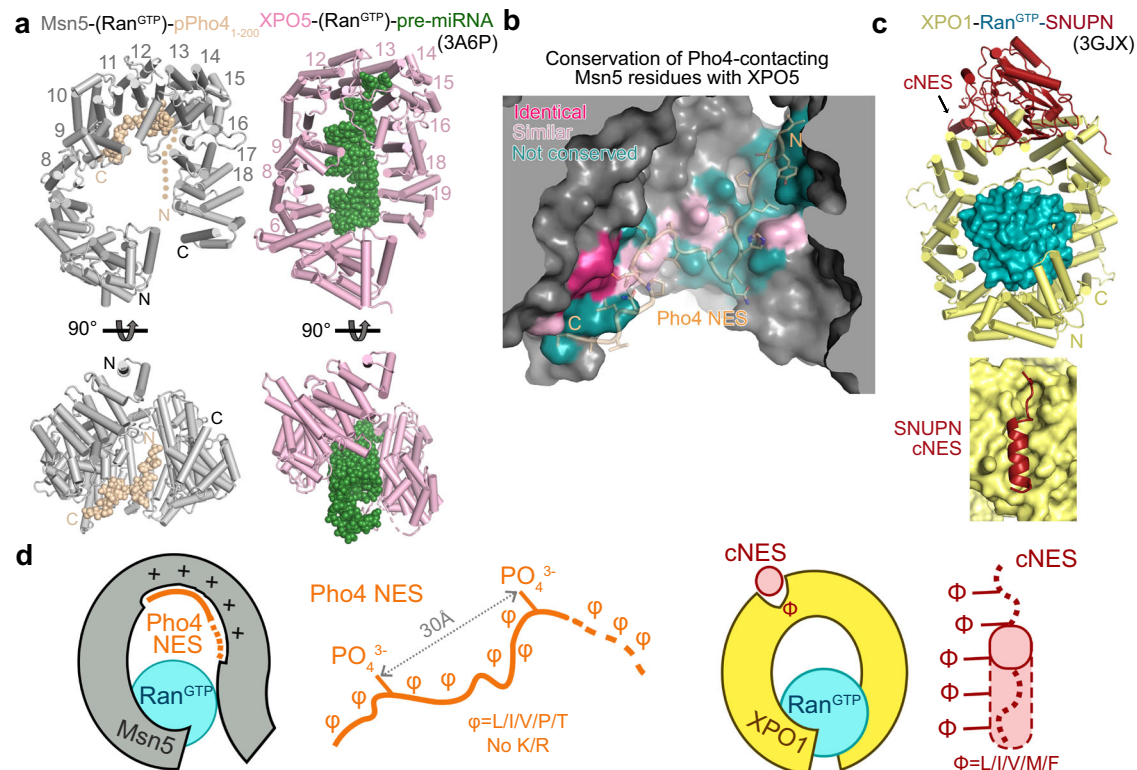


Fig. 5 | Comparison of cargo-bound Msn5 with XPO5 and XPO1. **a** Alignment of Ran^{GTP} in the Ran/cargo-bound structures Msn5 (grey) and XPO5 (pink; 3A6P [<https://doi.org/10.2210/pdb3A6P/pdb>]). Ran^{GTP} is omitted for clear view of the cargoes, which are drawn as spheres - pPho4 in wheat and pre-miRNA in green. HEAT repeats that contact the cargoes are labeled with their numbers. **b** Cargo-bound Msn5 and XPO5 shown in **a** are structurally aligned using DALI and the conservation of Msn5 residues that contact pPho4 are shown on the pPho4₁₋₂₀₀-bound Msn5 surface. Bound pPho4 is shown as transparent cartoon and sticks. Msn5 residues that contact pPho4 are colored dark pink if identical with the corresponding XPO5 residue, light pink if similar and dark teal if not conserved. **c** Top: XPO1 (yellow)-Ran^{GTP} (teal)-SNUPN (red) (3GJX [<https://doi.org/10.2210/pdb3GJX/pdb>]) oriented as in (a). Bottom: View of the SNUPN cNES in the NES binding groove of XPO1 (viewing in the direction of arrow in the top panel). **d** Cartoon summarizing Msn5-Pho4 NES (left) *vs.* XPO1-cNES (right) recognition. The Pho4 NES is an extended 35-amino acids-long chain with two phospho-serines spaced 14 residues (30 Å) apart and many small hydrophobic and polar residues. It is depleted of basic side chains as it interacts with the highly basic and flexible concave surface of Msn5. In contrast, the cNES is short (8–15 residues long), with 4–5 hydrophobic side chains that bind in a hydrophobic groove located on the convex surface of XPO1. The groove holds the same conformation as it binds structurally variable cNESs (dashed lines depict variability, solid line shows the structurally conserved single turn of helix).

with a large, open and expansive concave surface of its karyopherin, the Pho4 NES exhibits a more diffuse mode of karyopherin-signal recognition. This contrasts with the more compact and energy-concentrated interaction seen with monopartite classical NLSs^{28,73} and cNESs.

In addition to these structural features, the mechanism by which phosphorylated cargoes are recognized by their karyopherins remains poorly understood. The only other nuclear targeting signal known to be phosphorylated for karyopherin engagement is the arginine-serine (RS) NLS, which is recognized by the importin TNPO3/Transportin-SR^{74–76}. Interestingly, some RS-NLSs do not require phosphorylation, as they contain phosphomimetic sequences, such as the RS-like domain in CPSF6 protein⁷⁷. RS-NLSs are also complex, typically binding TNPO3 through both an IDR or linear element containing RPS repeats and a folded, globular RNA-recognition motif (RRM) domain^{75,77}. It remains unclear whether other Msn5 cargoes rely solely on their Pho4-like NESs for Msn5 binding or if the NES can function in conjunction with protein or RNA domains.

The different complexity of karyopherin recognition may also reflect the distinct cellular roles for different nuclear export pathways. For instance, the Pho4 NES and the classical NES may have evolved to export cargoes that are regulated in distinct ways in the cell. The narrowly defined affinity range for active nuclear export of Msn5 cargoes suggests that phosphorylation of either of the two critical sites within the NES tightly controls Pho4 export by Msn5. In contrast to the

broad, three orders of magnitude for XPO1-cNES active nuclear export, the Msn5 system may be better suited for more precise and rapid regulation of nuclear-cytoplasmic localization in response to environmental signals.

Msn5 autoinhibition, pPho4/Ran^{GTP} positive cooperativity and Pho4 release

We also solved the cryo-EM structure of unliganded Msn5 to 3.4 Å resolution. The structure suggests that the unliganded Msn5 is less flexible than Pho4-bound exportin (Fig. 6a, Table 1 and Supplementary Fig. 15). Unliganded Msn5 is a closed ring that involves extensive intramolecular interactions (Supplementary Fig. 16). The unliganded Msn5 ring is more compact than the most compact pPho4/Ran^{GTP}-bound Msn5 solenoid and resembles its human homolog XPO5 (SYU7 and 3A6P)^{38,78} (overlays in Supplementary Fig. 17). Three regions of Msn5 are significantly different in the unliganded Msn5 *versus* Msn5-Ran^{GTP}-pPho4₁₋₂₀₀ structures: h15loop, h17loop and the C-terminal helix and tail extension beyond h20 (C-helix-tail) (Fig. 6a). AlphaFold successfully predicted the closed ring structure of Msn5 but failed to predict the conformations of h15loop and h17loop (more on AF analysis in Supplementary Note 4).

The Ran^{GTP}-binding site at the N-terminal h1-h4 repeats of the Msn5-Ran^{GTP}-pPho4₁₋₂₀₀ structure is occupied by HEAT repeats h17-h20 and the C-helix-tail in the unliganded Msn5 structure (Fig. 6a). Both h15loop and h17loop also contact Ran^{GTP} in the former (Fig. 1a and

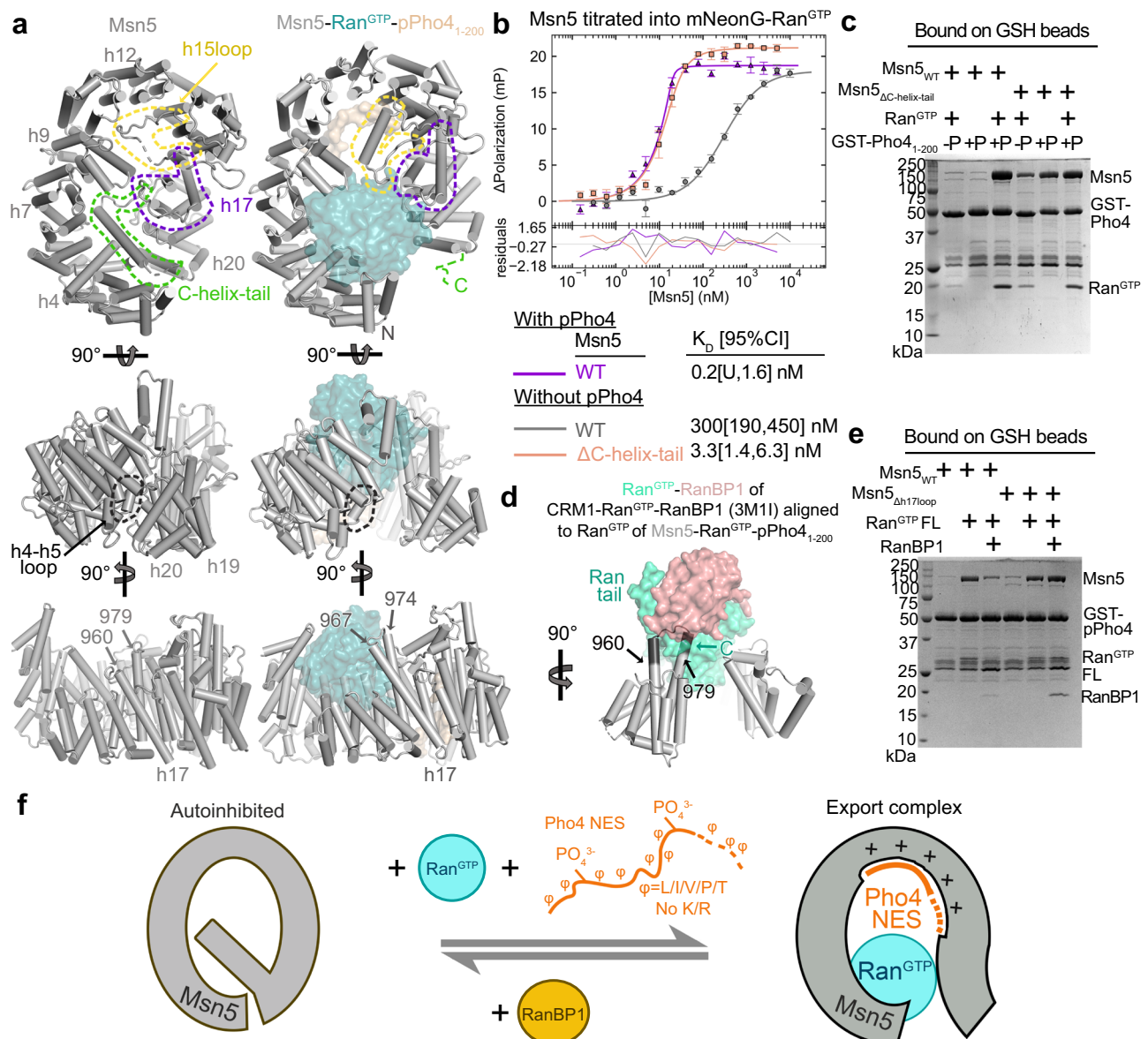


Fig. 6 | Unliganded Msn5 and the mechanisms for loading/unloading Pho4.

a Unliganded Msn5 (gray, left) and Msn5-Ran^{GTP}-pPho4₁₋₂₀₀ (gray-teal-wheat, right). Structural differences at h15loop, h17 and C-helix-tail are highlighted by yellow, purple and green dashed lines, respectively. The h4-h5loop that contacts h19-h20 in unliganded Msn5 but not in ligand-bound Msn5, is highlighted with black dashed lines. **b** FP titration of Msn5 WT or mutant ΔC-helix-tail to mNeonG-Ran^{GTP} ± excess pPho4₁₋₂₀₀. Data points are mean and s.d. of triplicate measurements, fitted with 1-site fitting (solid line) and fitting residuals are plotted below. **c** Bound proteins (after extensive washing) in an in vitro pull-down assay of immobilized unphosphorylated (-P) or phosphorylated GST-Pho4₁₋₂₀₀ (+P) incubated with Msn5

(WT or ΔC-helix-tail) ± Ran^{GTP}, visualized by Coomassie stained SDS-PAGE. Gel image from the single experiment is shown. **d** Msn5 (gray; h17 residues 960-979 in dark gray)-Ran^{GTP}-pPho4₁₋₂₀₀ and CRM1-Ran^{GTP}-RanBP1 (3MII) [<https://doi.org/10.2210/pdb3MII/pdb>)] structures aligned at Ran^{GTP}. CRM1 and pPho4 are not displayed for clearer visualization of the docked Ran^{GTP}-RanBP1 (aquamarine and pink, respectively). **e** As in **c**, pull-down assay of GST-pPho4₁₋₂₀₀ incubated with Msn5 WT or Δh17loop (residues 962-980 replaced with GGSGGS) ± Ran^{GTP} FL ± RanBP1 as labeled. Gel image from the single experiment is shown. **f** Cartoon model of cargo loading and unloading. Source data for **b**, **c** and **e** are provided as a Source Data file.

Supplementary Fig. 7b), and they undergo conformational changes when Msn5 is unliganded. These structural differences suggest that large conformational changes accompany Ran^{GTP} binding.

The NES binding site (h8-h18) of unliganded Msn5 is substantially more compact, occluding the groove at h12-h15 that binds region 2 and 3 of the Pho4 NES (Supplementary Fig. 17c). The same Msn5 region is also the hinge for conformational changes that result in the multiple states of Pho4-bound Msn5, some of which do not interact persistently with the Pho4 NES region 2 (Supplementary Figs. 5, 6). Interestingly, the dominant phospho-serine binding Msn5 RR site appears fully accessible in unliganded Msn5, potentially allowing initial partial binding of the Pho4 NES (Supplementary Fig. 17c). These structural

differences suggest that the unliganded conformation is incompatible with high affinity Pho4 NES binding which requires engagement of both phosphoserines in NES regions 2 and 4. Unliganded Msn5 is thus autoinhibited.

The autoinhibited conformation of unliganded Msn5 is consistent with weaker binding to either Ran^{GTP} or cargo alone. The K_D for Msn5 binding to mNeonG-Ran^{GTP} alone is 300 [190,450] nM compared to the sub-nanomolar K_D in the presence of pPho4₁₋₂₀₀; Msn5 is also not pulled-down by immobilized GST-pPho4₁₋₂₀₀ unless Ran^{GTP} is present (Fig. 6b, c, Supplementary Fig. 18). These results show positive cooperativity of cargo and Ran^{GTP} binding, typical of exportin systems. The binding of either pPho4 or Ran^{GTP} would

stabilize Msn5 conformations with separated N/C-termini, increasing affinity for the other ligand. The C-helix-tail that seems to hold together the termini of unliganded Msn5 may stabilize the autoinhibited state (Fig. 6a). Indeed, removal of the C-helix-tail (Msn5_{ΔC-helix-tail}; residues 1179–1224 removed) increased Ran^{GTP} binding affinity by 100-fold (K_D 3.3[1.4, 6.3] nM for Msn5_{ΔC-helix-tail} vs K_D 300 nM for WT Msn5; Fig. 6b). Immobilized GST-pPho4_{1–200} also pulled-down Msn5_{ΔC-helix-tail} even when Ran^{GTP} is absent (Fig. 6c). Thus, the C-helix-tail of Msn5 is key for stabilizing its autoinhibited state.

We examined the conformational changes at h17loop (residues 960–979) in more detail. This segment adopts a loop structure reaching over to h9-10loop in the unliganded structure; whereas in the Pho4/Ran^{GTP}-bound Msn5, residues 960–967 and 974–979 are helical and extend helices h17A and h17B, respectively, with the later segment contacting the Switch I of Ran^{GTP} (Fig. 6a). The Ran^{GTP} C-terminal tail is expected to become ordered upon binding the Ran^{GTP}-binding protein RanBP1, which is known to be important for releasing cargoes from XPO1^{79,80}. Alignment of Ran^{GTP}-RanBP1 from the XPO1-bound structure (3MI1⁷⁹ [<https://doi.org/10.2210/pdb3MI1/pdb>]) with the Ran^{GTP} of Msn5-Ran^{GTP}-pPho4_{1–200} reveals a steric clash between the Msn5 h17loop-extended h17B helix with the superimposed Ran tail and RanBP1 (Fig. 6d). This observation suggests that RanBP1-binding might destabilize the Msn5-Ran^{GTP}-pPho4 complex. Indeed, addition of RanBP1 (Sc Yrb1 Δ1–61) to Msn5 and Ran^{GTP} abolished binding to GST-pPho4_{1–200} (Fig. 6e). When the Msn5 h17loop residues, which are predicted to clash with Ran^{GTP}-RanBP1, are replaced with a GGSGGS linker, the mutant Msn5_{Δh17loop} can be captured by GST-pPho4_{1–200} in complex with both Ran^{GTP} and RanBP1 (Fig. 6e). These results suggest that the h17loop of Msn5 is likely the allosteric switch that causes Ran^{GTP} release from Msn5 upon RanBP1-binding, and thus Pho4 (and other NES cargo) release.

A cartoon model in Fig. 6f summarizes the mechanisms for loading and unloading cargo pPho4 onto Msn5. Unliganded Msn5 adopts an autoinhibited conformation where its C-helix-tail closes the solenoid ring⁷⁸. Ran^{GTP} binding displaces the C-helix-tail, opening the Msn5 solenoid to allow pPho4 to bind. Conformational changes of the Msn5 h17loop likely couples RanBP1-binding to Ran^{GTP} and cargo release to terminate a nuclear export cycle.

We have demonstrated that the 35-residue phosphorylated NES of Pho4 represents a non-classical class of linear NESs, distinct from the previously characterized XPO1-recognized NESs, and elucidated the mechanism by which it is recognized by Msn5. The Pho4 NES has two critical phosphorylated serine residues and many small- to medium-sized hydrophobic and polar residues that all contribute to Msn5-binding. Knowledge of Msn5-binding elements and the recognition mode explains the mechanisms of nuclear export regulation by Pho4 phosphorylation. It also suggests criteria for other Msn5 cargoes even though the large and open Msn5 surface with multiple potential phospho-serine/threonine binding sites likely accommodates diverse NESs. The partially conserved binding surface of the homologous XPO5 may recognize even more divergent NESs. Finally, unliganded Msn5 is an autoinhibited closed-ring solenoid, and comparison with Ran^{GTP} and Pho4-bound Msn5 explains the positive cooperativity of Ran^{GTP} and cargo binding typical of exportins and cargo release by RanBP1.

Methods

Cloning of constructs

All yeast protein expression constructs were cloned from the *S. cerevisiae* Genomic DNA library (Novagen Cat. 69240-3) using the primers listed in Supplementary Data 2. The construct expressing the Msn5 protein was cloned into a pQE60 vector (C-terminal His-tag) along with a TEV cleavage sequence for removal of the His-tag. Another construct expressing the Msn5 protein was also cloned into a pET28a vector (Novagen Cat. 69864), with TEV cleavage site after a N-terminal His-tag

inserted using NdeI and XhoI (New England Biolabs Cat. R0111 and R0146) and annealed TEV primers. The construct expressing truncated Msn5 proteins were generated by blunt end ligations. To generate the pET28a-Tev-mNeonG-Ran^{GTP} construct, pET28a-tev-mNeonG was first subcloned by inserting mNeonGreen from pLOM-S-mNeonGreen-EC18153 into BamHI-HF (New England Biolabs Cat. R3136) and XhoI sites. The construct expressing Ran^{GTP} or the *S. cerevisiae* Gsp1 residues 1–179, Q71L was expressed from a pET21d vector (NheI-HF and XhoI sites; New England Biolabs Cat. R3131). The construct expressing full length Pho4 protein was cloned into the pGex-Tev vector using restriction enzymes BamHI and XhoI. The construct expressing C-terminal Pho4 proteins were generated through insertions of stop codons. The construct expressing GST-Pho4_{100–150} was generated with blunt end ligation. The construct expressing Pho4_{3–200} was inserted into pET28a-Tev-mNeonG vector, using blunt end on one side, and XhoI on the other, to generate pET28a-Tev-mNeonG-Pho4_{FL} construct. C-terminal truncation was performed to generate pET28a-Tev-mNeonG-Pho4_{3–200} using blunt end ligations. All mutants were generated by either site-directed mutagenesis or blunt end ligations. The constructs expressing His-Pho85 and Pho80 were cloned into MCS-1 and -2 of the pRSFDuet vector using restriction enzymes BamHI-HF with NotI-HF (New England Biolabs Cat. R0189) and NdeI with XhoI, respectively.

For site-directed mutagenesis, amplification was performed using Phusion polymerase (Thermo Fisher Cat. F530), followed by DpnI (New England Biolabs Cat. R0176) cleavage for 1 hr in 37 °C before transformation into DH5α cells (Thermo Fisher Cat. EC0112) and plated on Luria Broth Agar plates with the appropriate antibiotic. For blunt end ligations, amplification was performed using Phusion polymerase, followed by DpnI cleavage for 1 hr in 37 °C and purified using Monarch PCR and DNA cleanup Kit (New England Biolabs Cat. T1030). 50 ng of the eluted vector is ligated alone, or with 1:3 molar ratio eluted inserts, with T4 DNA Ligase in the presence of T4 Polynucleotide Kinase (omitted if phosphorylated primers are used for amplification) at room temperature for 1.5 hr before transformation into DH5α cells and plated. All clones used in this study were verified by Sanger sequencing using primers that cover the region of interest (default T4 promoter/terminator, pGex forward or reverse, or specific primers as listed in Supplementary Data 2).

Msn5 expression and purification

All protein purification steps in this study were performed at 4 °C unless otherwise stated. All Msn5 constructs were transformed into Rosetta 2(DE3) cells (Novagen Cat. 71397) and grown in 6 L of Luria Broth media (RPI Cat. L24400) at 37 °C with 100 mg/mL ampicillin (RPI Cat. A40040) and 25 mg/mL chloramphenicol (Milipore Sigma Cat. C0378) until it reaches OD_{600nm} of 0.6. Expression was induced with 0.5 mM (for pQE60) or 0.25 mM (for pET28a) IPTG (Goldbio Cat. I2481) for 12 hr at 18 °C. Cells were spun down and resuspended with buffer A containing 50 mM HEPES pH 7.4 (Milipore Sigma Cat. H3375), 500 mM sodium chloride (RPI Cat. S23025), 10 % (v/v) glycerol (Milipore Sigma Cat. G7891), supplemented with 2 mM 2-mercaptoethanol (Milipore Sigma Cat. 444203), 1 mM benzamide (Milipore Sigma Cat. 434760), 10 μg/mL leupeptin (Alfa Assar Cat. J61188) and 50 μg/mL AEBSF (Goldbio Cat. A540) before use. The resuspension was lysed with an EmulsiFlex-C5 (Avestin) at ~10,000 psi and clarified by centrifugation at 48,400 g. The supernatant was supplemented with 10 mM imidazole pH 7.8 (Milipore Sigma Cat. 792527) and incubated with nickel beads (Qiagen Cat. 30210) for 10 – 30 min. Beads were washed with buffer A supplemented with 10 mM imidazole, 2 mM 2-mercaptoethanol and Msn5-His was eluted with buffer A containing 500 mM imidazole, 2 mM 2-mercaptoethanol. The elution was loaded onto HiTrap Phenyl HP column (Cytiva Cat. 17519501) and eluted with buffer containing 50 mM HEPES pH 7.4, 1 mM DTT (Goldbio Cat. DTT10) and 10 % glycerol over 50 mL at 2 mL/min. Elution was

concentrated to <10 mL and 1 mg of recombinant purified Tev was added to Msn5-His and incubated overnight. Tev-cleaved Msn5 was further purified in Superdex 200 Increase 10/300 GL column (Cytiva Cat. 28990944) in buffer B containing 20 mM HEPES pH 7.4, 150 mM sodium chloride, 10 % glycerol and 2 mM TCEP at 0.7 mL/min, concentrated using Amicon Ultra Centrifugal Filters (Millipore Sigma), and flash-frozen in liquid nitrogen and stored in -80°C .

Ran^{GTP} expression and purification

Ran^{GTP} is expressed using pET21d-Ran^{GTP} construct containing yeast Ran, Gsp1, residues 1-179 with Q71L mutation to stabilize the GTP bound form, and no manual GTP loading is needed. It is expressed and purified as described previously with the addition of TEV cleavage⁸¹. Briefly, Ran^{GTP}-His was expressed in 2 L of BL21(DE3) cells (New England Biolabs Cat. C2527) using 0.5 mM IPTG for 12 hr at 20°C . Cells were resuspended in buffer containing 50 mM HEPES pH 7.4, 2 mM magnesium acetate (Millipore Sigma Cat. 228648), 200 mM sodium chloride, 10 % glycerol, 5 mM imidazole pH 7.8, 2 mM 2-mercaptoethanol, 1 mM benzamidine, 10 $\mu\text{g/mL}$ leupeptin, 50 $\mu\text{g/mL}$ AEBSF. It was then lysed and clarified by centrifugation, and the supernatant was incubated with nickel beads before it was washed and eluted with 50 mM HEPES pH 7.4, 2 mM magnesium acetate, 50 mM sodium chloride, 10 % glycerol, 250 mM imidazole pH 7.8, 2 mM 2-mercaptoethanol. The elution was concentrated, and 1 mg of TEV was added for incubation overnight at 4°C . TEV-cleaved Ran^{GTP} was purified by ion-exchange using HiTrap SP HP column (Cytiva Cat. 17115201) over a gradient of 25 to 500 mM sodium chloride at 2 mL/min over 25 column volumes and clean protein was flash-frozen and stored in -80°C .

His-mNeonG-Ran^{GTP} was purified using 1 L of Rosetta(DE3)pLysS cells (Novagen Cat. 70956) grown with 50 mg/mL kanamycin (Caisson Labs Cat. K003) and 25 mg/mL chloramphenicol. Expression was induced with 0.25 mM IPTG at 18°C for 12 hr. Purification was performed like TEV-cleaved Ran^{GTP} to cleave off the His tag.

Ran^{GTP} FL-His was expressed using pET15b-Ran^{GTP} FL in 2 L of BL21 Gold(DE3) (Agilent Cat. 230132) cells with 0.5 mM IPTG for 3.5 hr at 37°C and purified as in human Ran FL in an established protocol⁸². Purification is similar to Ran^{GTP} but the His tag is left intact and protein is subjected to final purification in Superdex 75 10/300 column (Cytiva Cat. 17517401) in Buffer B instead. GTP is loaded on Ran^{GTP} FL by incubating the protein with 2 mM GTP (Millipore Sigma Cat. G8877) and 10 mM EDTA pH 8.0 (RPI Cat. E57020) for 40 min on ice, and addition of 40 mM magnesium acetate directly before use.

RanBP1 expression and purification

GST-RanBP1 was expressed in 2 L of BL21(DE3) cells using pGex-tev-RanBP1 (yeast Yrb1, residues 61-201) with 0.5 mM IPTG at 25°C for 10 hr and purified according to established protocol⁸¹. In short, cells were lysed in buffer containing 40 mM HEPES pH 7.5, 2 mM magnesium acetate, 200 mM sodium chloride, 10 mM DTT, 1 mM benzamidine, 10 $\mu\text{g/mL}$ leupeptin, 50 $\mu\text{g/mL}$ AEBSF and clarified, and supernatant was bound to glutathione Sepharose beads and washed with 100 mM and 300 mM sodium chloride. GST-RanBP1 was eluted with 30 mM GSH and cleaved with TEV overnight at 4°C . Reaction was passed over GSH beads again before it was purified over Superdex 75 similarly as Msn5.

Pho4 expression and purification

All GST-Pho4 constructs were transformed into BL21(DE3) cells and grown in 2 L of LB with 100 mg/mL ampicillin. Expression was induced with 0.5 mM IPTG at 25°C for 12 hr for GST-Pho4_{FL} or 30°C for 3.5 hr for GST-Pho4₁₋₂₀₀ variants. mNeonG-Pho4 variants were expressed like mNeonG-Ran^{GTP}.

Cells with GST proteins were lysed in buffer A supplemented with 2 mM DTT, 1 mM benzamidine, 10 $\mu\text{g/mL}$ leupeptin and 50 $\mu\text{g/mL}$ AEBSF, clarified and bound to glutathione Sepharose beads (Cytiva

Cat. 17075604), with the exception of GST-Pho4_{FL} where HEPES pH 7.5 was replaced with Tris pH 8.0 (RPI Cat. T60040). Beads were washed with the same buffer and eluted with buffer containing 25 mM sodium chloride and supplemented with 30 mM GSH (Millipore Sigma Cat. G4251). GST-Pho4_{FL} was further purified by HiTrap Q HP column (Cytiva Cat. 17115301) in 20 mM Tris pH 8.0, 10 % glycerol, 2 mM DTT using a gradient of 25 mM – 1 M sodium chloride at 2 mL/min over 25 column volumes. To generate Pho4^{FL}, beads were washed with buffer containing 20 mM Tris pH 8.0, 10 % glycerol, 150 mM sodium chloride, 1 mM DTT and 1 mg TEV was added to perform cleavage on-beads for 2 hr at room temp. Flowthrough was purified in Q column like GST-Pho4_{FL} but in Tris pH 8.5. GST-Pho4₁₋₂₀₀ eluted from beads was purified by Q in HEPES 7.0. Pho4₁₋₂₀₀ is generated in a similar manner as Pho4_{FL} but the Q is performed in HEPES pH 7.4.

Cells expressing His-mNeonG-Pho4₁₋₂₀₀ proteins were lysed in buffer A in Tris pH 8.0 with 10 mM imidazole pH 7.8, 2 mM 2-mercaptoethanol, 1 mM benzamidine, 10 $\mu\text{g/mL}$ leupeptin and 50 $\mu\text{g/mL}$ AEBSF and clarified. Supernatants were purified over HisTrap HP (Cytiva) in 50 mM Tris pH 8.0, 150 mM sodium chloride, 10 % glycerol, 10 – 150 mM imidazole pH 7.8, 2 mM 2-mercaptoethanol. Fractions containing His-mNeonG-Pho4₁₋₂₀₀ were concentrated and cut with Tev overnight to remove the His tag before further purification over Q column in HEPES pH 7.0 like the GST proteins and frozen. All Pho4 mutants expressed and behaved similarly during all steps of purification as the wild-type protein, suggesting that the mutations have preserved the physical property of Pho4 and did not induce aberrant aggregation or instability.

In vitro phosphorylation of Pho4

His-Pho85 and Pho80 were expressed using pRSFDuet vector mentioned above in 1 L of Rosetta(DE3)pLys cells using 1 mM IPTG at 18 or 25°C for 12 hr. Cells were lysed in buffer containing 20 mM HEPES pH 7.4, 150 mM sodium chloride, 10 % glycerol, 1 mM 2-mercaptoethanol and 40 mM imidazole pH 7.8, then clarified, and the supernatant was incubated with nickel beads. Beads were washed with 80 mM Imidazole and His-Pho85/Pho80 complex was eluted with 300 mM Imidazole. The complex was further purified over Superdex Increase S200 in buffer containing 20 mM HEPES pH 7.4, 150 mM sodium chloride, 10 % glycerol, 1 mM DTT and 10 mM magnesium chloride.

10 – 30 μM of Pho4 variants were mixed with 0.5 mM His-Pho85/Pho80 and ATP at 300 times the substrate concentration in 50 mM HEPES pH 7.4, 150 mM sodium chloride, 1 mM DTT, 10 mM magnesium chloride (Sigma-Aldrich Cat. M8266), 10% glycerol, and incubated at room temp for 1 hr. Proteins for pulldown binding assays were bound to beads for 10 min on ice and washed, while proteins for fluorescence polarization measurements were buffer exchanged on a Superdex 75 into buffer B using Amicon concentrators. Samples before and after phosphorylation was sent to intact mass analysis to ensure that phosphorylation was complete for all Pho4 variants that were used in this study (Supplementary Fig. 1e, 9f).

In vitro pull-down binding assays

For Fig. 1, 1 μM Msn5, 5 μM Ran^{GTP} and 1–2 μM GST proteins were mixed in buffer B in 200 μL reactions with 10–20 μL glutathione Sepharose beads and rotated at 4°C for 30 mins. Samples were then spun at 6000 xg for 1 min and flowthrough was removed. Buffer B was used to wash the beads for 3 times, 500 μL each. Lastly, 20 μL 2X SDS sample buffer was added to beads and boiled for 3 mins and bound proteins were visualized on SDS-PAGE gel for Coomassie staining. 2.5 μM GST-Pho4₁₋₂₀₀ or GST-pPho4₁₋₂₀₀ + 1 μM Msn5 (WT or mutants) \pm 5 μM Ran^{GTP} for assay in Fig. 6c, or 2.5 μM GST-pPho4₁₋₂₀₀ + 1 μM Msn5 \pm 5 μM Ran^{GTP} FL \pm 5 μM RanBP1 for assay in Fig. 6e, were assembled and treated the same way as described above. For binding assay in Supplementary Fig. 1c, GST-Pho4 proteins were expressed and purified in small scale (35 mL). Lysate was sonicated over nice before they were

clarified and bound to GSH beads and washed. Beads were used directly for binding assay with 5 μ M Msn5 and 20 μ M Ran^{GTP} following procedures described above.

Cryo-EM sample preparation and data collection

Complexes were formed by mixing Msn5, Ran^{GTP} and phosphorylated Pho4 in 1: 10:2 ratio and purified over Superdex S200 Increase in 20 mM HEPES pH 7.4, 150 mM sodium chloride, 2 mM magnesium acetate, 2 mM TCEP (Goldbio Cat. TCEP25). Msn5-Ran^{GTP}-pPho4₁₋₂₀₀ was diluted to 3.7 mg/mL and supplemented with 0.05 % NP-40 (Thermo-Fisher Cat. 85124). Msn5-Ran^{GTP}-pPho4_{FL} was diluted to 3 mg/mL and supplemented with 0.00125 % NP-40. Msn5 was diluted to 6 mg/mL in 20 mM HEPES pH 7.4, 150 mM sodium chloride, 2 mM TCEP with a final concentration of 0.1 % NP-40. Samples were applied on holey carbon grids (Quantifoil R1.2/1.3, 300 mesh copper) that were previously glow-discharged using a PELCO easiGlow glow discharge apparatus for 60 s at 30 mA (Ted Pella), and then plunge frozen using the Vitrobot Mark IV System (Thermo Fisher). One grid with best particle distribution for pPho4₁₋₂₀₀-containing complex was used for 48 hr data collection on a Titan Krios microscope equipped with K3 detector at the Cryo Electron Microscopy Facility (CEMF) at UT Southwestern Medical Center and yielded 12,474 movies at pixel size of 0.417 Å in super-resolution counting mode. Two different grids for pPho4_{FL}-containing complex were shipped to Pacific Northwest Cryo-EM Center (PNCC) for 72 hr data collection on the Titan Krios microscope equipped with K3 detector. A total of 13,496 movies were acquired from one grid at pixel size of 0.5115 Å in super-resolution counting mode. Two different Msn5 grids with best particle distribution were shipped to PNCC for 48 h data collection. A total of 8490 movies were acquired from the two grids collected the same way as the pPho4_{FL} sample.

Cryo-EM data processing

All data processing was performed using the software cryoSPARC v3.3.1 and v3.3.2 using default parameters⁸³. A 1/2 F-crop factor was applied during patch motion correction, followed by patch CTF estimation. For Msn5-Ran^{GTP}-pPho4₁₋₂₀₀, blob picker was used to select 3,752,564 initial particles, which cleaned up to 1,574,329 particles after one round of 2D classification. After additional 9 extensive rounds of 2D classification, 883,743 particles were used to obtain 3 ab initio models, which were subsequently submitted to heterogeneous refinement. ~30% of the particles partitioned into a map that looks like Msn5 alone. The rest of the particles, a total of 617,333 particles can be further refined using non-uniform refinement to generate a 2.97 Å resolution map which showed clearly density for Ran^{GTP} but not Pho4. These particles were then further used to generate 6 new ab initio models which were then submitted to heterogeneous refinement and non-uniform refinement with per-particle defocus and per-group CTF optimization. These 6 reconstructions were classified into different states based on visual inspection and map alignment in ChimeraX v1.4⁸⁴.

Msn5-Ran^{GTP}-pPho4_{FL} was processed similarly and had 1,104,150 particles after a single round of 2D classification. After 7 additional rounds of 2D classification, 395,996 particles were classified into 6 classes, only 2 of which with most particles looked like good particles and were submitted to non-uniform refinement without per-particle defocus and per-group CTF optimization to yield two maps of ~ 5 Å resolution. The resulting 2 reconstructions were classified into different states based on visual inspection and map alignment in ChimeraX with the 6 maps obtained for Msn5-Ran^{GTP}-pPho4₁₋₂₀₀.

For unliganded Msn5, blob picker was used to select initial particles which cleaned up to 4,135,768 after one 2D classification run. After 6 rounds of 2D classification, 1,450,905 particles were used to generate 6 ab initio models. Some junk classes were observed, therefore more particles (1,998,715 particles from one less round of 2D classification)

were submitted for heterogeneous refinement with three input models which included two bad classes to sink junk particles. The best map of 3.39 Å resolution was obtained by further non-uniform refinement of a subset of 1,048,421 particles, with per-particle defocus and per-group CTF refinement. Including the other subset of particles (which looked highly similar) did not improve resolution.

Cryo-EM model building, refinement and analysis

Unsharpened maps were used for model building as they have the best overall features. SWISS-MODEL was used to generate an initial 3D-model of Msn5 using Exportin-5 structure as a template (PDB ID: 5YU7⁷⁸ [<https://doi.org/10.2210/pdb5YU7/pdb>]). The Msn5 model and Ran^{GTP} from PDB ID 3MII⁷⁹ [<https://doi.org/10.2210/pdb3MII/pdb>] were fitted into the State-1-1 map using UCSF ChimeraX, followed by multiple cycles of manual model building using ISOLDE⁸⁵ in ChimeraX, Coot v0.9⁸⁶ and real-space refinement in Phenix v1.20⁸⁷. This map has poor density for the last two HEAT repeats at the C-terminal, and the last two HEAT repeats were modeled by merging with a fragment of a docked model of Msn5 alone. The Msn5 from the State 1-1 structure is used as input model for States 2-1 and States 3-1, where Msn5 is first split into three segments, one split at h12 and one at h17 and fitted in Chimera. In both State 2-1 and State 3-1 maps, the density for Pho4 is not well-defined and too ambiguous for modeling (see more in Supplementary Note 1), and therefore we have not modeled any Pho4 residues in the final deposited models. Model validation was performed in Phenix. The binding interfaces were analyzed using CONTACT/ACT in CCP4 with cut-off of 4.0 Å⁸⁸. These interactions were curated and analyzed in PyMOL 2.4.2 where the final figures were generated⁸⁹. Map images were generated in ChimeraX.

Fluorescence Polarization assays

Fluorescence polarization assays were performed in the same way as previously described⁸¹. In brief, triplicates of sixteen 20 μ L samples were assembled with final concentration of 20 nM mNeonG-pPho4₁₋₂₀₀, 30 μ M Ran^{GTP} and a 1:1 serially diluted wild type or mutant Msn5 from 10 μ M, in a 384 well black bottom plate (Corning). For Ran^{GTP} binding affinities, samples contain 20 nM mNeonG-Ran^{GTP} with serial dilution of wild type or mutant Msn5 from 10 μ M. Measurements were performed in a CLARIOstar Plus plate reader (BMG Labtech) using the CLARIOstar software v 5.20 RS with top optics using excitation filter 482-16, dichroic filter LP 504 and emission filter 530-40, 50 flashes per well. Gain was optimized to target mP of ~220 for mNeonG-pPho4₁₋₂₀₀ and ~200 for mNeonG-Ran^{GTP}. Data was outputted using the MARS software v3.10 R6 and analyzed in PALMIST v1.5.8⁹⁰ and plotted in GUSI v1.4.2⁹¹.

RNAseq sample preparation, data collection and processing

Msn5 was cloned into a p413 yeast expression vector (His selection) with a Cyc1 promoter inserted and the HRYRR_{AAAAA} mutants were generated by PCR using WT vector. The ASY788 strain (*Msn5* knockout) was acquired from Martha S. Cyert's Lab and transformed with either an empty p413 vector, a p413 WT *Msn5* vector, or a p413 HRYRR_{AAAAA} *Msn5* mutant vector. Colonies were assessed for proper incorporation by plating on synthetic complete medium agar plates without Histidine, so only cells carrying the plasmids conferring the His selection marker would grow. Single colonies were taken directly off the plate and inoculated into 5 mL overnight YPAD (yeast, peptone, adenine, glucose) cultures and grown to mid-log phase. Cultures were spun down, washed twice with PBS, pelleted and flash frozen prior to downstream processing. Each strain was grown in triplicate.

Total RNA from each pellet was extracted using the Monarch Total RNA Miniprep Kit (New England Biolabs Cat. T2010). In brief, pellets were resuspended in 1X DNA/RNA protection reagent, glass beads were added to the resuspension before vortexing at high speed to lyse. Samples were spun down and supernatant was spun through a column

to remove gDNA. Flowthrough was mixed with ethanol to facilitate binding to an RNA purification column, onto which samples were subjected to DNase I treatment, before being washed several times and eluted in nuclease-free water. Illumina mRNA-seq library preps were conducted by The Rockefeller University Genomics core facility. Samples were pooled and analyzed with a NextSeq 2000 instrument with high output flowcell 75 single read sequencing.

Initial sequencing data was processed in Linux, starting with the FastQC software v0.12.0 used to check the quality of the raw data. Poor quality regions and adapter sequences were trimmed using Trimmomatic v0.39. Reads were aligned to the *Saccharomyces cerevisiae* genome (acquired from *Saccharomyces* Genome Database) using STAR v2.7.11a. Finally gene hit counts were determined using FeatureCounts v2.0.6. Normalized counts of all genes and fold effects are included in Source Data. Comparison of hit counts between conditions and any further downstream analysis was conducted using R scripting. Comparison between conditions was conducted using DESeq2 v1.40.2 and volcano plots were generated using ggplot2.

Growth curve assays

pRS414 vectors carrying the powerful ADHI promoter and either no gene, the wild type *Msn5* or the *Msn5* HRYRR_{AAAA} double mutant were transformed into the ASY788 strain. These new strains were inoculated in 5 mL of YPAD medium and grown overnight. The OD600 values of the saturated overnight cultures were determined, and each strain diluted to a starting OD600 of 0.0025. Four replicate wells of a 96-well plate (Corning Cat. 3997) were grown for each growth curve, along with four blank wells of just YPAD medium as a baseline OD600 reading. The prepared plate was placed in a Tecan Spark plate reader and OD600 values were collected every 15 min for 24 h under maximum orbital agitation using Tecan plate reader data acquisition software Spark Control v3.2. Three separate readings were collected per well at each time point and mean value determined for each well at a given time point. The mean value and standard deviation of the four replicate wells for each strain were determined to plot the growth curve.

Reporting summary

Further information on research design is available in the Nature Portfolio Reporting Summary linked to this article.

Data availability

The cryoEM map and structures generated in this study have been deposited in PDB under accession codes [9D45](#), [9DXM](#), [9DZ6](#) and [9D43](#); and in EMDB under accession codes [EMD-46549](#), [EMD-47291](#), [EMD-47325](#), [EMD-46548](#), [EMD-46556](#), [EMD-46557](#), [EMD-46560](#), [EMD-46561](#) and [EMD-46562](#). RNAseq data have been deposited in the NCBI BioSample database as SRA experiments under the accession code [PRJNA1215799](#). X-ray crystallography structure of previous studies used for making figures can be found in PDB under accession codes [5YU7](#), [3A6P](#), [3GJX](#), [3MII](#), [1WA5](#) and [3ICQ](#). AlphaFold2 model of Pho4 and Msn5 can be found in AlphaFold Protein Structure Database with the accession code AF-P07270-F1 [<https://alphafold.ebi.ac.uk/entry/P07270>] and AF-P52918-F1 [<https://alphafold.ebi.ac.uk/entry/P52918>]. Source data are provided with this paper.

References

- Flores, K., Yadav, S. S., Katz, A. A. & Seger, R. The nuclear translocation of mitogen-activated protein kinases: Molecular mechanisms and use as novel therapeutic target. *Neuroendocrinology* **108**, 121–131 (2019).
- Chen, X. & Xu, L. Mechanism and regulation of nucleocytoplasmic trafficking of smad. *Cell Biosci.* **1**, 40 (2011).
- Kofler, M. & Kapus, A. Nuclear Import and Export of YAP and TAZ. *Cancers (Basel)* **15** <https://doi.org/10.3390/cancers15204956> (2023).
- Wing, C. E., Fung, H. Y. J. & Chook, Y. M. Karyopherin-mediated nucleocytoplasmic transport. *Nat. Rev. Mol. Cell Biol.* **23**, 307–328 (2022).
- Yang, Y. et al. Nuclear transport proteins: structure, function, and disease relevance. *Signal Transduct. Target Ther.* **8**, 425 (2023).
- Chang, C. C. & Hsia, K. C. More than a zip code: global modulation of cellular function by nuclear localization signals. *FEBS J.* **288**, 5569–5585 (2021).
- Kaffman, A., Rank, N. M., O'Neill, E. M. & Huang, L. S. & O'Shea, E. K. The receptor Msn5 exports the phosphorylated transcription factor Pho4 out of the nucleus. *Nature* **396**, 482–486 (1998).
- Mahanty, S. K., Wang, Y., Farley, F. W. & Elion, E. A. Nuclear shuttling of yeast scaffold Ste5 is required for its recruitment to the plasma membrane and activation of the mating MAPK cascade. *Cell* **98**, 501–512 (1999).
- DeVit, M. J. & Johnston, M. The nuclear exportin Msn5 is required for nuclear export of the Mig1 glucose repressor of *Saccharomyces cerevisiae*. *Curr. Biol.* **9**, 1231–1241 (1999).
- Blondel, M. et al. Nuclear export of Far1p in response to pheromones requires the export receptor Msn5p/Ste21p. *Genes Dev.* **13**, 2284–2300 (1999).
- Komeili, A., Wedaman, K. P., O'Shea, E. K. & Powers, T. Mechanism of metabolic control. Target of rapamycin signaling links nitrogen quality to the activity of the Rtg1 and Rtg3 transcription factors. *J. Cell Biol.* **151**, 863–878 (2000).
- Boustany, L. M. & Cyert, M. S. Calcineurin-dependent regulation of Crz1p nuclear export requires Msn5p and a conserved calcineurin docking site. *Genes Dev.* **16**, 608–619 (2002).
- Gorner, W. et al. Acute glucose starvation activates the nuclear localization signal of a stress-specific yeast transcription factor. *EMBO J.* **21**, 135–144 (2002).
- Jaquenoud, M., van Drogen, F. & Peter, M. Cell cycle-dependent nuclear export of Cdh1p may contribute to the inactivation of APC/C(Cdh1). *EMBO J.* **21**, 6515–6526 (2002).
- Kaplun, L., Ivantsiv, Y., Bakhrat, A. & Raveh, D. DNA damage response-mediated degradation of Ho endonuclease via the ubiquitin system involves its nuclear export. *J. Biol. Chem.* **278**, 48727–48734 (2003).
- Queralt, E. & Igual, J. C. Cell cycle activation of the Swi6p transcription factor is linked to nucleocytoplasmic shuttling. *Mol. Cell Biol.* **23**, 3126–3140 (2003).
- Quan, X., Tsoulos, P., Kuritzky, A., Zhang, R. & Stochaj, U. The carrier Msn5p/Kap142p promotes nuclear export of the hsp70 Ssa4p and relocates in response to stress. *Mol. Microbiol.* **62**, 592–609 (2006).
- Ueta, R., Fujiwara, N., Iwai, K. & Yamaguchi-Iwai, Y. Mechanism underlying the iron-dependent nuclear export of the iron-responsive transcription factor Aft1p in *Saccharomyces cerevisiae*. *Mol. Biol. Cell* **18**, 2980–2990 (2007).
- Towpik, J., Graczyk, D., Gajda, A., Lefebvre, O. & Boguta, M. Derepression of RNA polymerase III transcription by phosphorylation and nuclear export of its negative regulator, Maf1. *J. Biol. Chem.* **283**, 17168–17174 (2008).
- Wagner, M. V. et al. Whi5 regulation by site specific CDK-phosphorylation in *saccharomyces cerevisiae*. *PLoS One* **4**, e4300 (2009).
- Quilis, I. & Igual, J. C. Molecular basis of the functional distinction between Cln1 and Cln2 cyclins. *Cell Cycle* **11**, 3117–3131 (2012).
- Taberner, F. J., Quilis, I., Sendra, J., Bano, M. C. & Igual, J. C. Regulation of cell cycle transcription factor Swi5 by karyopherin Msn5. *Biochim Biophys. Acta* **1823**, 959–970 (2012).

23. Sugiyama, M. et al. Nuclear localization of Haa1, which is linked to its phosphorylation status, mediates lactic acid tolerance in *Saccharomyces cerevisiae*. *Appl Environ. Microbiol.* **80**, 3488–3495 (2014).
24. Strahl, T., Hama, H., DeWald, D. B. & Thorner, J. Yeast phosphatidylinositol 4-kinase, Pik1, has essential roles at the Golgi and in the nucleus. *J. Cell Biol.* **171**, 967–979 (2005).
25. Kaffman, A., Herskowitz, I. & Tjian, R. & O'Shea, E. K. Phosphorylation of the transcription factor PHO4 by a cyclin-CDK complex, PHO80-PHO85. *Science* **263**, 1153–1156 (1994).
26. Komeili, A. & O'Shea, E. K. Roles of phosphorylation sites in regulating activity of the transcription factor Pho4. *Science* **284**, 977–980 (1999).
27. O'Neill, E. M., Kaffman, A., Jolly, E. R. & O'Shea, E. K. Regulation of PHO4 nuclear localization by the PHO80-PHO85 cyclin-CDK complex. *Science* **271**, 209–212 (1996).
28. Soniat, M. & Chook, Y. M. Nuclear localization signals for four distinct karyopherin-beta nuclear import systems. *Biochem J.* **468**, 353–362 (2015).
29. Christie, M. et al. Structural biology and regulation of protein import into the nucleus. *J. Mol. Biol.* **428**, 2060–2090 (2016).
30. Fung, H. Y., Fu, S. C., Brautigam, C. A. & Chook, Y. M. Structural determinants of nuclear export signal orientation in binding to exportin CRM1. *Elife* **4** <https://doi.org/10.7554/eLife.10034> (2015).
31. Fung, H. Y., Fu, S. C. & Chook, Y. M. Nuclear export receptor CRM1 recognizes diverse conformations in nuclear export signals. *Elife* **6** <https://doi.org/10.7554/eLife.23961> (2017).
32. Guttler, T. et al. NES consensus redefined by structures of PKI-type and Rev-type nuclear export signals bound to CRM1. *Nat. Struct. Mol. Biol.* **17**, 1367–1376 (2010).
33. Monecke, T. et al. Crystal structure of the nuclear export receptor CRM1 in complex with Snurportin1 and RanGTP. *Science* **324**, 1087–1091 (2009).
34. Dong, X. et al. Structural basis for leucine-rich nuclear export signal recognition by CRM1. *Nature* **458**, 1136–1141 (2009).
35. Stuvén, T., Hartmann, E. & Görlich, D. Exportin 6: a novel nuclear export receptor that is specific for profilin-actin complexes. *EMBO J.* **22**, 5928–5940 (2003).
36. Matsuura, Y. & Stewart, M. Structural basis for the assembly of a nuclear export complex. *Nature* **432**, 872–877 (2004).
37. Cook, A. G., Fukuhara, N., Jinek, M. & Conti, E. Structures of the tRNA export factor in the nuclear and cytosolic states. *Nature* **461**, 60–65 (2009).
38. Okada, C. et al. A high-resolution structure of the pre-microRNA nuclear export machinery. *Science* **326**, 1275–1279 (2009).
39. Aksu, M. et al. Xpo7 is a broad-spectrum exportin and a nuclear import receptor. *J. Cell Biol.* **217**, 2329–2340 (2018).
40. Baade, I., Spillner, C., Schmitt, K., Valerius, O. & Kehlenbach, R. H. Extensive identification and in-depth validation of importin 13 Cargo. *Mol. Cell Proteom.* **17**, 1337–1353 (2018).
41. Lipowsky, G. et al. Exportin 4: a mediator of a novel nuclear export pathway in higher eukaryotes. *EMBO J.* **19**, 4362–4371 (2000).
42. Ogawa, N. & Oshima, Y. Functional domains of a positive regulatory protein, PHO4, for transcriptional control of the phosphatase regulon in *Saccharomyces cerevisiae*. *Mol. Cell Biol.* **10**, 2224–2236 (1990).
43. Shimizu, T. et al. Crystal structure of PHO4 bHLH domain-DNA complex: flanking base recognition. *EMBO J.* **16**, 4689–4697 (1997).
44. Jayaraman, P. S., Hirst, K. & Goding, C. R. The activation domain of a basic helix-loop-helix protein is masked by repressor interaction with domains distinct from that required for transcription regulation. *EMBO J.* **13**, 2192–2199 (1994).
45. Byrne, M., Miller, N. & Springer, M. & O'Shea, E. K. A distal, high-affinity binding site on the cyclin-CDK substrate Pho4 is important for its phosphorylation and regulation. *J. Mol. Biol.* **335**, 57–70 (2004).
46. Ng, Y. W. et al. Why an A-loop phospho-mimetic fails to activate PAK1: understanding an inaccessible kinase state by molecular dynamics simulations. *Structure* **18**, 879–890 (2010).
47. Somale, D. et al. Activation of RSK by phosphomimetic substitution in the activation loop is prevented by structural constraints. *Sci. Rep.* **10**, 591 (2020).
48. Chu, N. et al. Akt kinase activation mechanisms revealed using protein semisynthesis. *Cell* **174**, 897–907 e814 (2018).
49. Zhou, X. X., Fan, L. Z., Li, P., Shen, K. & Lin, M. Z. Optical control of cell signaling by single-chain photoswitchable kinases. *Science* **355**, 836–842 (2017).
50. Niu, W., Li, Z., Zhan, W., Iyer, V. R. & Marcotte, E. M. Mechanisms of cell cycle control revealed by a systematic and quantitative overexpression screen in *S. cerevisiae*. *PLoS Genet* **4**, e1000120 (2008).
51. Douglas, A. C. et al. Functional analysis with a barcoder yeast gene overexpression system. *G3 (Bethesda)* **2**, 1279–1289 (2012).
52. Duffy, S. et al. Overexpression screens identify conserved dosage chromosome instability genes in yeast and human cancer. *Proc. Natl Acad. Sci. USA* **113**, 9967–9976 (2016).
53. Abramson, J. et al. Accurate structure prediction of biomolecular interactions with AlphaFold 3. *Nature* **630**, 493–500 (2024).
54. Holm, L. & Laakso, L. M. Dali server update. *Nucleic Acids Res* **44**, W351–W355 (2016).
55. Wu, K., He, J., Pu, W. & Peng, Y. The role of exportin-5 in MicroRNA biogenesis and cancer. *Genomics Proteom. Bioinforma.* **16**, 120–126 (2018).
56. Yi, R., Qin, Y., Macara, I. G. & Cullen, B. R. Exportin-5 mediates the nuclear export of pre-microRNAs and short hairpin RNAs. *Genes Dev.* **17**, 3011–3016 (2003).
57. Bohnsack, M. T., Czapinski, K. & Görlich, D. Exportin 5 is a RanGTP-dependent dsRNA-binding protein that mediates nuclear export of pre-miRNAs. *RNA* **10**, 185–191 (2004).
58. Gwizdek, C. et al. Exportin-5 mediates nuclear export of minihelix-containing RNAs. *J. Biol. Chem.* **278**, 5505–5508 (2003).
59. Lund, E., Guttinger, S., Calado, A., Dahlberg, J. E. & Kutay, U. Nuclear export of microRNA precursors. *Science* **303**, 95–98 (2004).
60. Chatterjee, K., Marshall, W. A. & Hopper, A. K. Three tRNA nuclear exporters in *S. cerevisiae*: parallel pathways, preferences, and precision. *Nucleic Acids Res* **50**, 10140–10152 (2022).
61. Hopper, A. K. & Nostramo, R. T. tRNA processing and subcellular trafficking proteins multitask in pathways for other RNAs. *Front Genet* **10**, 96 (2019).
62. Calado, A., Treichel, N., Muller, E. C., Otto, A. & Kutay, U. Exportin-5-mediated nuclear export of eukaryotic elongation factor 1A and tRNA. *EMBO J.* **21**, 6216–6224 (2002).
63. Bohnsack, M. T. et al. Exp5 exports eEF1A via tRNA from nuclei and synergizes with other transport pathways to confine translation to the cytoplasm. *EMBO J.* **21**, 6205–6215 (2002).
64. Brownawell, A. M. & Macara, I. G. Exportin-5, a novel karyopherin, mediates nuclear export of double-stranded RNA binding proteins. *J. Cell Biol.* **156**, 53–64 (2002).
65. Macchi, P. et al. The brain-specific double-stranded RNA-binding protein Staufen2: nucleolar accumulation and isoform-specific exportin-5-dependent export. *J. Biol. Chem.* **279**, 31440–31444 (2004).
66. Gwizdek, C. et al. Minihelix-containing RNAs mediate exportin-5-dependent nuclear export of the double-stranded RNA-binding protein ILF3. *J. Biol. Chem.* **279**, 884–891 (2004).
67. Wild, T. et al. A protein inventory of human ribosome biogenesis reveals an essential function of exportin 5 in 60S subunit export. *PLoS Biol.* **8**, e1000522 (2010).

68. Mingot, J. M., Vega, S., Cano, A., Portillo, F. & Nieto, M. A. eEF1A mediates the nuclear export of SNAG-containing proteins via the Exportin5-aminoacyl-tRNA complex. *Cell Rep.* **5**, 727–737 (2013).
69. Kosugi, S., Yanagawa, H., Terauchi, R. & Tabata, S. NESmapper: accurate prediction of leucine-rich nuclear export signals using activity-based profiles. *PLoS Comput Biol.* **10**, e1003841 (2014).
70. Fu, S. C., Fung, H. Y. J., Cagatay, T., Baumhardt, J. & Chook, Y. M. Correlation of CRM1-NES affinity with nuclear export activity. *Mol. Biol. Cell* **29**, 2037–2044 (2018).
71. Zhang, Z. C. & Chook, Y. M. Structural and energetic basis of ALS-causing mutations in the atypical proline-tyrosine nuclear localization signal of the Fused in Sarcoma protein (FUS). *Proc. Natl Acad. Sci. USA* **109**, 12017–12021 (2012).
72. Gonzalez, A. et al. A new Karyopherin-beta2 binding PY-NLS epitope of HNRNP2 linked to neurodevelopmental disorders. *Structure* **31**, 924–934 e924 (2023).
73. Lu, J. et al. Types of nuclear localization signals and mechanisms of protein import into the nucleus. *Cell Commun. Signal* **19**, 60 (2021).
74. Lai, M. C., Lin, R. I. & Tarn, W. Y. Transportin-SR2 mediates nuclear import of phosphorylated SR proteins. *Proc. Natl Acad. Sci. USA* **98**, 10154–10159 (2001).
75. Maertens, G. N. et al. Structural basis for nuclear import of splicing factors by human Transportin 3. *Proc. Natl Acad. Sci. USA* **111**, 2728–2733 (2014).
76. Yun, C. Y., Velazquez-Dones, A. L., Lyman, S. K. & Fu, X. D. Phosphorylation-dependent and -independent nuclear import of RS domain-containing splicing factors and regulators. *J. Biol. Chem.* **278**, 18050–18055 (2003).
77. Jang, S. et al. Differential role for phosphorylation in alternative polyadenylation function versus nuclear import of SR-like protein CPSF6. *Nucleic Acids Res* **47**, 4663–4683 (2019).
78. Yamazawa, R. et al. Structural basis for selective binding of export cargoes by exportin-5. *Structure* **26**, 1393–1398 e1392 (2018).
79. Koyama, M. & Matsuura, Y. An allosteric mechanism to displace nuclear export cargo from CRM1 and RanGTP by RanBP1. *EMBO J.* **29**, 2002–2013 (2010).
80. Kehlenbach, R. H., Dickmanns, A., Kehlenbach, A., Guan, T. & Gerace, L. A role for RanBP1 in the release of CRM1 from the nuclear pore complex in a terminal step of nuclear export. *J. Cell Biol.* **145**, 645–657 (1999).
81. Fung, H. Y. J. & Chook, Y. M. Binding affinity measurement of nuclear export signal peptides to their exporter CRM1. *Methods Mol. Biol.* **2502**, 245–256 (2022).
82. Fung, H. Y. J. & Chook, Y. M. Crystallization of nuclear export signals or small-molecule inhibitors bound to nuclear exporter CRM1. *Methods Mol. Biol.* **2502**, 285–297 (2022).
83. Punjani, A., Rubinstein, J. L., Fleet, D. J. & Brubaker, M. A. cryoSPARC: algorithms for rapid unsupervised cryo-EM structure determination. *Nat. Methods* **14**, 290 (2017).
84. Pettersen, E. F. et al. UCSF ChimeraX: Structure visualization for researchers, educators, and developers. *Protein Sci.* **30**, 70–82 (2021).
85. Croll, T. I. ISOLDE: a physically realistic environment for model building into low-resolution electron-density maps. *Acta Crystallogr D. Struct. Biol.* **74**, 519–530 (2018).
86. Emsley, P. New tools for ligand refinement and validation in coot and CCP4. *Acta Crystallogr A* **74**, A390–A390 (2018).
87. Adams, P. D. et al. PHENIX: a comprehensive Python-based system for macromolecular structure solution. *Acta Crystallogr D.* **66**, 213–221 (2010).
88. Winn, M. D. et al. Overview of the CCP4 suite and current developments. *Acta Crystallogr D. Biol. Crystallogr* **67**, 235–242 (2011).
89. Schrodinger, L. L. C. *The PyMOL Molecular Graphics System, Version 2.4* (2020).
90. Scheuermann, T. H., Padrick, S. B., Gardner, K. H. & Brautigam, C. A. On the acquisition and analysis of microscale thermophoresis data. *Anal. Biochem.* **496**, 79–93 (2016).
91. Brautigam, C. A. Calculations and publication-quality illustrations for analytical ultracentrifugation data. *Methods Enzymol.* **562**, 109–133 (2015).

Acknowledgements

pLOM-S-mNeonGreen-EC18153 was a gift from Julian Hibberd (Addgene plasmid #137075; <http://n2t.net/addgene:137075>; RRI-D:Addgene_137075). pRSFDuet-1 vector was a gift from Christopher P. Hill. The ASY788 Msn5 knockout strain was a gift from Martha S. Cyert. We thank Yang Li, Yan Han and Zhe Chen at Structural Biology Laboratory, the CEMF in UTSW, and Sean Mulligan and Harry Scott at PNCC for their expert assistance with Cryo-EM data collection. We also thank the Erzberger lab for using their plate reader for FP. We thank Michael McConville and Glen Liszczak for synthesizing phosphorylated peptides. SBL and CEMF at UTSW are partially supported by grant RP220582 from the Cancer Prevention & Research Institute of Texas (CPRIT). We thank the Genomics Resource Center at The Rockefeller University for assistance in mRNA sequencing library prep and data collection. A portion of this research was supported by NIH grant U24GM129547 and performed at the PNCC at OHSU and accessed through EMSL (grid.436923.9), a DOE Office of Science User Facility sponsored by the Office of Biological and Environmental Research. Molecular graphics and analyses performed with UCSF ChimeraX, developed by the Resource for Biocomputing, Visualization, and Informatics at the University of California, San Francisco, with support from National Institutes of Health R01-GM129325 and the Office of Cyber Infrastructure and Computational Biology, National Institute of Allergy and Infectious Diseases. This work was funded by NIGMS of NIH under Awards R35GM141461 (Y.M.C.), R01GM069909 (Y.M.C.), P41GM109824, R01 CA228351 and R01 GM112108 (M.P.R.), the Welch Foundation Grants I-1532 (Y.M.C.), support from the Alfred and Mabel Gilman Chair in Molecular Pharmacology, Eugene McDermott Scholar in Biomedical Research (Y.M.C.) and the Gilman Special Opportunities Award (H.Y.J.F.).

Author contributions

Conceptualization, Y.M.C.; Methodology, Y.M.C., M.P.R., H.Y.J.F., S.R.M., A.E.C., T.Y.; Investigation, H.Y.J.F., S.R.M., A.N., J.J., B.S., A.E.C., T.Y.; Writing—Original Draft, H.Y.J.F., S.R.M.; Writing—Review & Editing, Y.M.C., H.Y.J.F., M.P.R., S.R.M.; Funding Acquisition, Y.M.C. and M.P.R.

Competing interests

The authors declare no competing interests.

Additional information

Supplementary information The online version contains supplementary material available at <https://doi.org/10.1038/s41467-025-57752-3>.

Correspondence and requests for materials should be addressed to Yuh Min Chook.

Peer review information *Nature Communications* thanks Yun Zhu and the other, anonymous, reviewer(s) for their contribution to the peer review of this work. A peer review file is available.

Reprints and permissions information is available at <http://www.nature.com/reprints>

Publisher's note Springer Nature remains neutral with regard to jurisdictional claims in published maps and institutional affiliations.

Open Access This article is licensed under a Creative Commons Attribution-NonCommercial-NoDerivatives 4.0 International License, which permits any non-commercial use, sharing, distribution and reproduction in any medium or format, as long as you give appropriate credit to the original author(s) and the source, provide a link to the Creative Commons licence, and indicate if you modified the licensed material. You do not have permission under this licence to share adapted material derived from this article or parts of it. The images or other third party material in this article are included in the article's Creative Commons licence, unless indicated otherwise in a credit line to the material. If material is not included in the article's Creative Commons licence and your intended use is not permitted by statutory regulation or exceeds the permitted use, you will need to obtain permission directly from the copyright holder. To view a copy of this licence, visit <http://creativecommons.org/licenses/by-nc-nd/4.0/>.

© The Author(s) 2025